Article

Iron-containing nickel cobalt sulfides, selenides and a sulfoselenide as active and stable electrocatalysts for the oxygen evolution reaction in alkaline solution

Soheil Abdpour [1], Lars Rademacher [1], Marcus. N. A. Fetzer [1], Thi Hai Yen Beglau[1], Christoph Janiak [1,*]

[1] Institut für Anorganische Chemie und Strukturchemie, Heinrich-Heine-Universit¨at Düsseldorf, 40204 Düsseldorf, Germany; soheil.abdpour@hhu.de (S.A); larad101@hhu.de (L.R);,marcus.fetzer@uni-duesseldorf.de (M.F); beglau@uni-duesseldorf.de (T.H.Y.B.); Janiak@hhu.de (C.J)

* Correspondence: Janiak@hhu.de

Abstract: Iron-containing nickel sulfides, selenides, and sulfoselenides were synthesized via a simple two-step hydrothermal reaction (temperature ≤ 160 °C) for their application as electrocatalysts in the oxygen evolution reaction (OER) in an alkaline solution (1 mol L^{-1} KOH). The study demonstrated that iron-containing nickel cobalt sulfides and selenides exhibit superior OER performance with lower overpotentials compared to iron-free nickel cobalt sulfide and selenide, which highlights the significant role of iron in enhancing OER nickel cobalt electrocatalysts: $Fe_{0.1}Ni_{1.4}Co_{2.9}(S_{0.87}O_{0.13})_4$, η_{50} = 318 mV; $Fe_{0.2}Ni_{1.5}Co_{2.8}(S_{0.9}O_{0.1})_4$, η_{50} = 310 mV; $Fe_{0.3}Ni_{1.2}Co_{2.5}(S_{0.9}O_{0.1})_4$, η_{50} = 294 mV; $Fe_{0.6}Ni_{1.2}Co_{2.5}(S_{0.83}O_{0.17})_4$, η_{50} = 294 mV, $Fe_{0.4}Ni_{0.7}Co_{1.6}(Se_{0.81}O_{0.19})_4$, η_{50} = 306 mV compared to $Ni_{1.0}Co_{2.1}(S_{0.9}O_{0.1})_4$, η_{50} = 346 mV and $Ni_{0.7}Co_{1.4}(Se_{0.85}O_{0.15})_4$, η_{50} = 355 mV (all values at current densities η_{50} of 50 mA cm^{-2}). Furthermore, the iron-containing nickel cobalt sulfoselenide $Fe_{0.5}Ni_{1.0}Co_{2.0}(S_{0.57}Se_{0.25}O_{0.18})_4$ displayed exceptional OER performance with η_{50} = 277 mV, surpassing the benchmark RuO_2 electrode with η_{50} = 299 mV. The superior performance of the sulfoselenide was attributed to its low charge transfer resistance (Rct) of 0.8 Ω at 1.5 V vs. the reversible hydrogen electrode (RHE). Moreover, the sulfoselenide demonstrated remarkable stability, with only a minimal increase in overpotential (η_{50}) from 277 mV to 279 mV after a 20 h chronopotentiometry test. These findings suggest that trimetallic iron, nickel and cobalt sulfide, selenide and especially sulfoselenide materials hold promise as high-performance, cost-effective, and durable electrocatalysts for sustainable OER reactions. This study provides a valuable approach for the development of efficient electrocatalytic materials, contributing to the advancement of renewable energy technologies.

Keywords: Iron-containing material, Nickel cobalt sulfide, Nickel cobald selenide, Sulfoselenide, Oxygen evolution reaction (OER.)

1. Introduction

According to the US Energy Information Administration (EIA) report, the total world energy consumption will rise to 815 quadrillion Btu (British thermal units) in 2040, a 29% increase compared to 2020 [1] , demonstrating the increasing demand for energy in the near future. Using clean and renewable energy is one of the main issues for societies. Green hydrogen (H_2), produced with renewable energy, is seen as an alternative fuel and energy storage resource in the future [2]. Water splitting is one of the most studied ways to produce H_2. With electrocatalysis, this process includes the hydrogen evolution reaction (HER) and the oxygen evolution reaction (OER) [3]. The anodic reaction (OER) involves a sluggish four-electron-proton coupled transfer reaction. It is the main obstacle to an economic water-splitting process since it requires a much higher potential (1.6-2 V vs. the reversible hydrogen electrode, RHE) than the theoretical equilibrium potential of E° = 1.23 V vs. RHE [4–8].

The well-known benchmark materials for OER are the oxides of iridium and ruthenium (IrO_2 and RuO_2), while Pt-based materials are used as benchmarks for HER [9].

Preprints (www.preprints.org) | NOT PEER-REVIEWED | Posted: 13 June 2023 doi:10.20944/preprints202306.0928.v1

However, the high cost, scarcity, and low stability of these precious noble metals limit their practical large-scale application for water electrolysis [10,11]. Sustainable water splitting requires utilizing non-precious metals as a catalyst. Using non-precious metals with high abundance, durability, and catalytic activity, especially in OER, can effectively improve the scalability of electrocatalytic hydrogen production. Therefore, in recent years, there has been an impetus to develop high-performance, stable, and low-cost (non-noble) transition metal-based electrocatalysts such as transition metal sulfides, hydroxides, oxides, oxide-hydroxides, phosphides, and nitrides for OER [12–18].

Transition metal sulfides possess good conductivity and excellent mechanical and thermal stability, making them promising electrocatalysts for OER and HER and the oxygen reduction reaction (ORR) [19]. Moreover, mixed-metal sulfides, MMSs, show even higher electric conductivity and richer redox reactions through the synergistic effect of multi-transition metal ions, leading to a notable enhancement in electrocatalytic performance compared to monometallic sulfides [20,21].

Bimetallic nickel cobalt sulfide is one of the most studied and promising MMSs, extensively studied for electrocatalytic energy conversion and storage devices [22]. For example, the thiospinel $NiCo_2S_4$ with Ni(II) on tetrahedral (T_d) sites and Co(III) ions on octahedral (O_h) sites receives much attention in many electrocatalysis applications, including water splitting, supercapacitors, and zinc-air batteries [23–26]. However, the electrocatalytic activity and stability of $NiCo_2S_4$ remain lower than IrO_2 and RuO_2 in OER and lower than Pt-based catalysts for HER [27]. To improve the electrocatalytic performance of nickel cobalt sulfides, researchers have applied many different strategies, including making composites with carbon materials [28–30], metal oxides [31,32], oxyhydroxides [24], layer double hydroxide [28], metal sulfides [33,34], incorporating other active metals such as Ru, Ir, and Pt in the structure [35,36] and also partially replacing sulfur ions with nitrogen [37], phosphorous [38] or selenium ions [39].

The improved electrocatalytic performance of nickel cobalt sulfide in the presence of anions such as Se and P can be attributed to effectively altering the surface electron density by modulating the compound's d-band [36,40,41]. Increased electrocatalytic activity in the presence of other cations is mainly related to improving exposed active sites, reducing the charge transfer resistance, enhancing structural stability, and synergistic interactions between host and guest cations [42,43].

Although replacing anions or cations is widely used to upgrade the water-splitting performance of nickel cobalt sulfides, only a few reports applied a simultaneous cation and anion replacement to evaluate a possible synergistic effect. Recently, Deng et al. synthesized the polymetallic sulfoselenide, $Co_{0.31}Ni_{0.22}Ru_{0.05}S_{0.46}Se_{0.41}$, which showed an overpotential of $\eta_{10} = 261$ mV (1.491 V vs. RHE) at 10 mA cm^{-2}, while RuO_2 needed $\eta_{10} = 254$ mV (1.484 V vs. RHE) at the same condition [44]. However, ruthenium limits its classification as a completely non-precious metal electrocatalyst.

Here we establish a facile two-step hydrothermal strategy to synthesize iron-containing nickel cobalt sulfides, selenides and sulfoselenide as non-precious polymetallic compounds. A series of mixed-metal iron nickel cobalt carbonate hydroxide hydrates, (Fe_xNi_{1-x})CoCH-(y), were synthesized and used as a precursor for sulfurization, selenization, and sulfoselenization.

2. Materials and Methods

2.1 Materials

All commercial chemicals were used as received without any purification. Cobalt chloride hexahydrate $CoCl_2{\cdot}6H_2O$ (CAS: 7791-13-1 98% abcr GmbH, Karlsruhe, Germany), nickel chloride hexahydrate $NiCl_2{\cdot}6H_2O$ (CAS: 7791-20-0 98%, ACS reagent, Roth, Karlsruhe, Germany), ammonium iron(II) sulfate hexahydrate $(NH_4)_2Fe(SO_4)_2{\cdot}6H_2O$ (CAS: 7783-85-9 BioUltra, 99% Sigma Aldrich, St. Louis, MO, USA), sodium sulfide nonahydrate $Na_2S{\cdot}9H_2O$ (CAS: 1313-84-4 98% Acros Organics, New Dehli, India), selenium dioxide SeO_2 (CAS: 7446-08-4 98%, Sigma Aldrich, St. Louis, MO, USA), urea $OC(NH_2)_2$ (CAS: 57-

Preprints (www.preprints.org) | NOT PEER-REVIEWED | Posted: 13 June 2023 doi:10.20944/preprints202306.0928.v1

13-6 ACS reagent 99.5%, Sigma Aldrich, St. Louis, MO, USA), potassium hydroxide KOH (CAS: 1310-58-3,1N, Roth, Karlsruhe, Germany), N-methyl-2-pyrrolidone NMP (CAS: 872-32-2 95%, abcr, Karlsruhe, Germany), hydrazine monohydrate $N_2H_4{\cdot}H_2O$ (CAS: 7803-57-8, Thermo Scientific, Kandel, Germany), polyvinylidene fluoride PVDF (CAS: 24937-79-9, Sigma Aldrich, Karlsruhe, Germany), carbon black Vulcan XC-72R (Fuelcellstore, Bryan , TX, USA). Nickel foam NF was purchased from Recemat BV, Cell Material Engineering, The Netherlands. Ultrapure water was produced using the Sartorius Arium mini device. Before using NF, it was cut into 1×2 cm^2 pieces and cleaned with acetone (CAS: 67-64-1, ACS reagent, ≥99.5%, Sigma Aldrich, St. Louis, MO, USA), hydrochloric acid (CAS: 7647-01-0, 1 mol L^{-1}, Geel, Belgium), ultrapure water, and ethanol (CAS: 64-17-5, 98%, Th. Geyer, Renningen, Germany) for 15 min in an ultrasonic bath and then dried at 100 °C in a vacuum oven for 15 min.

2.2 Preparation of nickel cobalt carbonate hydroxide (NiCoCH) and iron nickel cobalt carbonate hydroxide (Fe_xNi_{1-x})CoCH-(y) precursors

The NiCoCH sample was prepared according to the previously reported method by Chen et al. [20]. The amount of 950 mg (4.00 mmol) $CoCl_2{\cdot}H_2O$, 475 mg (2.00 mmol) $NiCl_2{\cdot}6H_2O$, and 1.1 g (18 mmol) urea was added to 40 mL of ultrapure water and stirred for 10 min. Then the obtained solution was transferred into a Teflon-lined stainless-steel autoclave and heated to 120 °C for 6 h. The product was washed five times with ultrapure water (50 mL each) and two times with ethanol (25 mL each), then dried in a vacuum oven at 60 °C overnight. Yield = 860 mg. (Fe_xNi_{1-x})CoCH-(y) precursors were synthesized by the same method except that the amounts of 98, 196, 294, or 392 mg (0.25, 0.50, 0.75, 1.0 mmol) of $(NH_4)_2Fe(SO_4)_2{\cdot}6H_2O$ were added. Yields = 875 mg, 900 mg, 917 mg, and 930 mg, respectively.

Hereafter (Fe_xNi_{1-x})CoCH-(y) was used to refer to the iron-containing nickel cobalt carbonate hydroxide with y = 0.25, 0.50, 0.75, and 1.0 mmol of $(NH_4)_2Fe(SO_4)_2{\cdot}6H_2O$ added to the reaction mixture, (Fe_xNi_{1-x})CoCH-(y) refers to all samples.

2.3 Preparation of iron nickel cobalt sulfides, selenide, and sulfoselenide

Iron-containing nickel cobalt sulfide samples were prepared by hydrothermal sulfidation of the (Fe_xNi_{1-x})CoCH-(y) precursors. A chosen amount of iron-containing precursor (125 mg) was dispersed in 40 mL of ultrapure water in an 80 mL Teflon-lined autoclave and stirred for 20 min. After that, 750 mg (3.125 mmol) of $Na_2S{\cdot}9H_2O$ was added. The resultant suspension was transferred to the oven, and the temperature was kept at 160 °C for 12 h. The obtained product was washed five times with ultrapure water (50 mL each) and two times with ethanol (20 mL each), then dried in a vacuum oven at 60 °C overnight. Yields about 90 mg.

The iron-containing nickel cobalt sulfoselenide sample, $Fe_{0.5}Ni_{1.0}Co_{2.0}(S_{0.57}Se_{0.25}O_{0.18})_4$, was synthesized via sulfidation and selenization of (Fe_xNi_{1-x})CoCH-(1.0) in one step. (Fe_xNi_{1-x})CoCH-(1.0) (125 mg) was dispersed in ultrapure water and stirred for 20 min. Then 680 mg (2.70 mmol) of $Na_2S{\cdot}9H_2O$ and 50 mg (0.425 mmol) of SeO_2 were added to the suspension. Finally, 10 mL of $N_2H_4{\cdot}H_2O$ was slowly added to the suspension. The Teflon-lined stainless-steel autoclave was kept at 160 °C for 12 h. The resulting powder was washed five times with ultrapure water (50 mL each time) and two times with ethanol (20 mL each time) and dried at 60 °C overnight. Yield 100 mg.

Iron-containing nickel cobalt selenide, $Fe_{0.4}Ni_{0.7}Co_{1.6}(Se_{0.81}O_{0.19})_4$ was synthesized by selenization of (Fe_xNi_{1-x})CoCH-(1.0). (Fe_xNi_{1-x})CoCH-(1.0) (125 mg) was dispersed in 30 mL of ultrapure water and stirred for 20 min followed by adding 100 mg (0.9 mmol) SeO_2. Then 10 mL of N_2H_4 was added to above mention suspension and stirred for another 10 min. The resulting suspension was transferred to a stainless autoclave and heated at 160 °C for 12 h. The obtained black powder was washed five times with ultrapure water (50 mL each) and three times with absolute ethanol (20 mL each), then dried at 60 °C in the vacuum oven overnight. Yield 110 mg.

For comparison, nickel cobalt sulfide, $Ni_{1.0}Co_{2.1}(S_{0.9}O_{0.1})_4$ and nickel cobalt selenide, $Ni_{0.7}Co_{1.4}(Se_{0.85}O_{0.15})_4$, and were synthesized by sulfidation or selenization, respectively of

Preprints (www.preprints.org) | NOT PEER-REVIEWED | Posted: 13 June 2023 doi:10.20944/preprints202306.0928.v1

NiCoCH respectively (Supplementary Materials, Section S1). The schematic illustration of the synthesis is shown in Scheme 1.

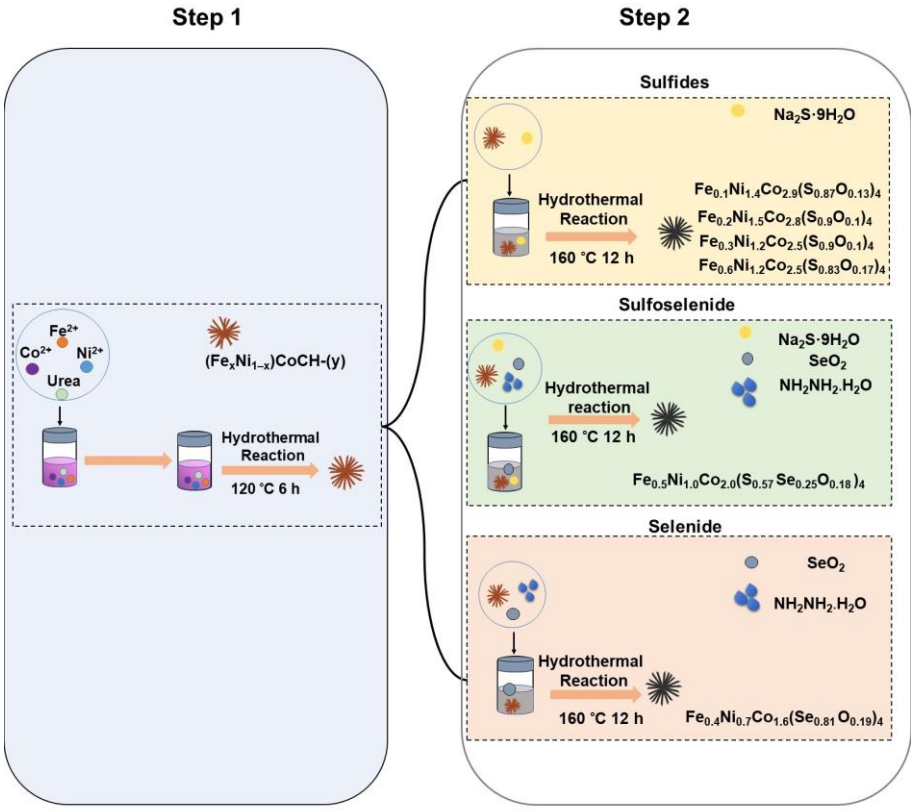

Scheme 1. Schematic illustration of the preparation process for iron-containing Ni-Co sulfide, sulfoselenide and selenide. (Fe$_x$Ni$_{1-x}$)CoCH-(y) represents the precursor iron-containing nickel cobalt carbonate hydroxide hydrate.

2.4 Material characterization

Powder X-ray diffraction (PXRD) analysis was conducted at ambient temperature on a Rigaku Miniflex 600 powder diffractometer (Rigaku, Tokyo, Japan) using Cu Kα1 radiation with λ = 1.5406 Å (40 kV, 15 mA, 600 W) and a flat silicon low background with a small indent in the range of 2θ = 5°–100°. The obtained PXRD data were evaluated with the Match 3.11 software.

Scanning electron microscopy (SEM) was performed with Jeol JSM-6510LV QSEM (Jeol, Akishima, Japan) advanced electron microscope (LaB_6 cathode at 20 kV) equipped with a Bruker Xflash 410 silicon drift detector for energy-dispersive X-ray (EDX) spectroscopy.

Transmission electron microscopy (TEM) with energy-dispersive X-ray spectroscopy (TEM-EDX) was carried out with a FEI Tecnai G2 F20 electron microscope (FEI Co., Hillsboro, OR, USA) operated at 200 kV accelerating voltage.

A Quantachrome Autosorb-6 automatic adsorption analyzer (Quantachrome Gmbh; Odelzhausen, Germany) was used to determine nitrogen sorption isotherms for the BET surface area determination of the samples at 77 K. The samples were degassed at 90 °C in a 10^{-2} mbar vacuum for 15 h before the gas sorption measurement.

X-ray photoelectron spectroscopy (XPS) data were collected using a ULVAC-PHI VersaProbe II microfocus X-ray photoelectron spectrometer (ULVAC-PHI, Chigasaki, Japan). The spectra were recorded using a polychromatic aluminum Kα X-ray source (1486.8 eV) and referenced to the carbon 1s orbital with a binding energy of 284.8 eV.

Quantification of the metal content of the samples was performed using a Perkin-Elmer PinaAcle 900T atomic absorption spectrometer (Perkin Elmer LAS GmbH, Rodgau-

Preprints (www.preprints.org) | NOT PEER-REVIEWED | Posted: 13 June 2023 doi:10.20944/preprints202306.0928.v1

Jügesheim, Germany) (sample preparation described in Supplementary Materials, Section S2).

The sulfur content was determined with a VarioMICRO CHNS microanalyzer (Elementar Analysensysteme, Langenselbold, Germany).

2.5 Electrochemical measurements

All electrochemical analyses were conducted on a three-electrode cell using an Interface 1010E potentiostat from Gamry Instruments at ambient temperature. The reversible hydrogen electrode, RHE, and Pt foil were used as a reference and counter electrode. Coated nickel foam, NF, was the working electrode. A slurry containing 8:1:1 mass portions of the active materials (mixed-metal sulfide, selenide, or sulfoselenide material), carbon black, Vulcan XC-72R, and polyvinylidene fluoride, PVDF, respectively, in *N*-methyl-2-pyrrolidone, NMP was prepared and carefully dropped on a ~1 cm^2 area of the NF surface, and dried at 60 °C for 12 h in a vacuum oven to prepare the coated NF electrode. Before starting the electrochemical analysis, an N_2 gas flow was passed through the electrolyte to remove dioxygen from the 1 mol L^{-1} KOH electrolyte.

Linear sweep voltammetry LSV measurement was applied to determine the catalytic performance of the coated NF electrode at a scan rate of 5 mV s^{-1}. Before starting the LSV measurement, 20 cycles of cyclic voltammetry at a scan rate of 100 mV s^{-1} were run to reach a stable electrocatalytic performance. The potentials of the LSV polarization curves were corrected by iR compensation. The chronopotentiometry at the current density of 50 mA cm^{-2} for 20 h was used to evaluate the stability of the selected electrocatalyst in long-term performance. Moreover, to understand the electrode/electrolyte interface behavior, electrochemical impedance spectroscopy, EIS, was performed in the frequency range of 0.1-100 kHz at 1.5 V vs. RHE.

3. Result and Discussion

3.1 Synthesis and analysis

Nickel cobalt carbonate hydroxide (NiCoCH) and iron-containing nickel cobalt carbonate hydroxides (Fe_xNi_{1-x})CoCH-(y) were synthesized from $CoCl_2{\cdot}6H_2O$, $NiCl_2{\cdot}6H_2O$, $(NH_4)_2Fe(SO_4)_2{\cdot}6H_2O$ and urea as precursors in hydrothermal reactions (Step 1 in Scheme 1). Four different amounts of $(NH_4)_2Fe(SO_4)_2{\cdot}6H_2O$ were used to synthesize (Fe_xNi_{1-x})CoCH-(y) while keeping the $NiCl_2{\cdot}6H_2O$ and $CoCl_2{\cdot}6H_2O$ amounts constant. The samples were named (Fe_xNi_{1-x})CoCH-(0.025), (Fe_xNi_{1-x})CoCH-(0.05), (Fe_xNi_{1-x})CoCH-(0.075), and (Fe_xNi_{1-x})CoCH-(0.1), representing the use of 0.025, 0.05, 0.075, and 1.0 mmol of the iron precursor. The sulfidation and selenization of the metal carbonate hydroxide precursors was achieved through a hydrothermal sulfidation process with $Na_2S{\cdot}9H_2O$ and a selenization process with SeO_2 (Step 2 in Scheme 1). For the sulfoselenide sample, a mixture of $Na_2S{\cdot}9H_2O$ and SeO_2 was employed in the hydrothermal reaction.

Two different methods were used to determine the chemical formula of the as-prepared samples, a combination of AAS for the metal and CHNS analysis for the sulfur content (method 1) and SEM-EDX (method 2) (Supplementary Materials, Table S2-S6). Method 1 provides more precise atomic ratios of metal and S content in the samples than EDX. In EDX the emitted X-rays give a 1-2 μm depth analysis but EDX as an X-ray spectroscopy experiences matrix effects and would need standards of similar composition as the sample for peak identification and accurate quantification. For the sulfoselenide and selenide sample, AAS for the metal content was combined with EDX for the Se content. Moreover, the chemical formulae obtained from AAS + CHNS + EDX were much closer to charge balance than the EDX-derived formulae. Based on the metal to sulfur ratios obtained from method 1 and the charge balance calculation of the samples, oxygen should also be incorporated into the structure of the samples. The presence of oxygen in the structure of samples was also proven from the EDX and XPS spectrum. Therefore, the chemical formulae are given here with their estimated oxygen content. The chemical formulas resulting from methods 1 and 2 are provided in Table S6. The measured SEM-EDX data of the samples are provided in Figures S1-S8.

Preprints (www.preprints.org) | NOT PEER-REVIEWED | Posted: 13 June 2023 doi:10.20944/preprints202306.0928.v1

The crystallinity of all sulfide samples was low, as evidenced by broad peaks of low intensity in the powder X-ray diffractograms, PXRDs (Figure 1a). The crystalline phases in the iron-containing nickel cobalt samples were verified as spinels by matching to the known diffractograms of $NiCo_2S_4$ (ICDD no. 43-1477) and Co_3S_4 (ICDD no. 75-1561) (Figure 1). The prominent diffraction peaks located at 26.8°, 31.5°, 38.1°, 50.4°, and 55.2° can be attributed to the (220), (311), (400), (511), and (440) planes of the spinel lattice [17]. In addition, in the PXRD patterns of $NiCo_2S_4$ and iron-containing nickel cobalt samples, the diffraction peaks at 29.9° and 52.1° can be attributed to the (311) and (440) planes, respectively, of Co_9S_8 (ICDD no. 73-1442). It should be mentioned that the presence of an Co_9S_8 impurity in $NiCo_2S_4$ is reported in much previous literature, including Chen et al. work [20], who first reported the formation of sea urchin-like $NiCo_2S_4$ using metal carbonate hydroxide as a precursor [30,37,45–48].

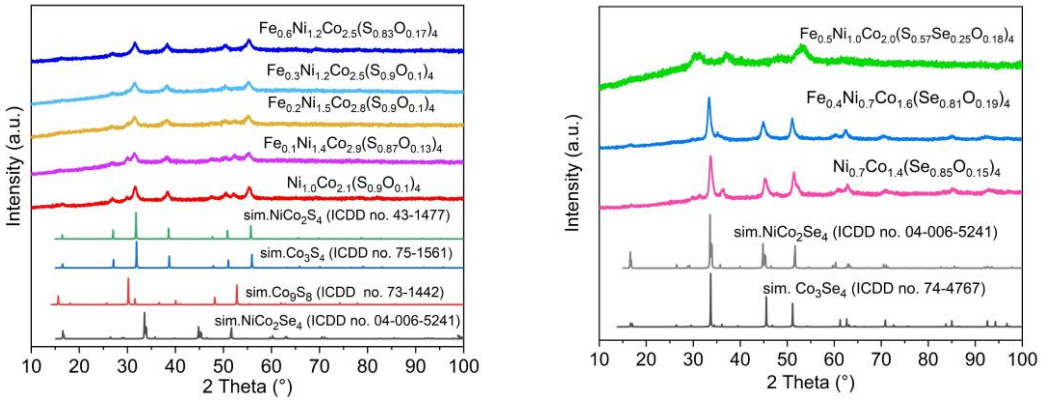

(a) **(b)**

Figure 1. PXRD patterns of **(a)** as-prepared sulfide and **(b)** selenide and sulfoselenide samples compared to simulated (sim.) patterns of different metal sulfides and selenides.

The content of the crystalline Co_9S_8 impurity decreases with increasing iron content and is only barely visible in $Fe_{0.3}Ni_{1.2}Co_{2.5}(S_{0.9}O_{0.1})_4$ and no longer visible in $Fe_{0.6}Ni_{1.2}Co_{2.5}(S_{0.83}O_{0.17})_4$. The corresponding selenides are of higher crystallinity (Figure 1b). The prominent reflection peaks of $NiCo_2Se_4$ and $Fe_{0.4}Ni_{0.7}Co_{1.6}(Se_{0.81}O_{0.19})_4$ match the simulation for $NiCo_2Se_4$ (ICDD no. 04-006-5241), where they correspond to the (002), (311), and (-313) crystal plane located at 33.3°, 44.9°, and 51.4°, respectively [49]. By incorporating both sulfur and selenium in the structure, the crystallinity of $Fe_{0.5}Ni_{1.0}Co_{2.0}(S_{0.57}Se_{0.25}O_{0.18})_4$ from the PXRD pattern became too low and no clear crystalline phase analysis was possible anymore. Such low crystallinity was also seen in the literature for nickel sulfoselenide, oxygen-containing cobalt sulfide, and nickel sulfide nanoparticles, which were reported with excellent OER properties [50–52].

The morphology of the as-prepared samples was studied using scanning electron microscopy, SEM. As shown in Figure 2a, $Ni_{1.0}Co_{2.1}(S_{0.9}O_{0.1})_4$ consists of needle-like structures combining parts with a sea urchin-like morphology. By increasing the iron content, the morphology became more sea urchin-like (Figure 2b-f). In the selenides and the sulfoselenide $Fe_{0.6}Ni_{1.2}Co_{2.5}(S_{0.83}O_{0.17})_4$ sample, Figure 2 e-f, agglomerations of needle-like primary particles can be seen. The SEM-energy dispersive X-ray (EDX) mappings (Supplementary Materials, Figure S9) support the AAS- and CHNS-based elemental analysis for the chemical formulae, and SEM-EDX was the analysis of choice to determine the selenium content.

Preprints (www.preprints.org) | NOT PEER-REVIEWED | Posted: 13 June 2023 doi:10.20944/preprints202306.0928.v1

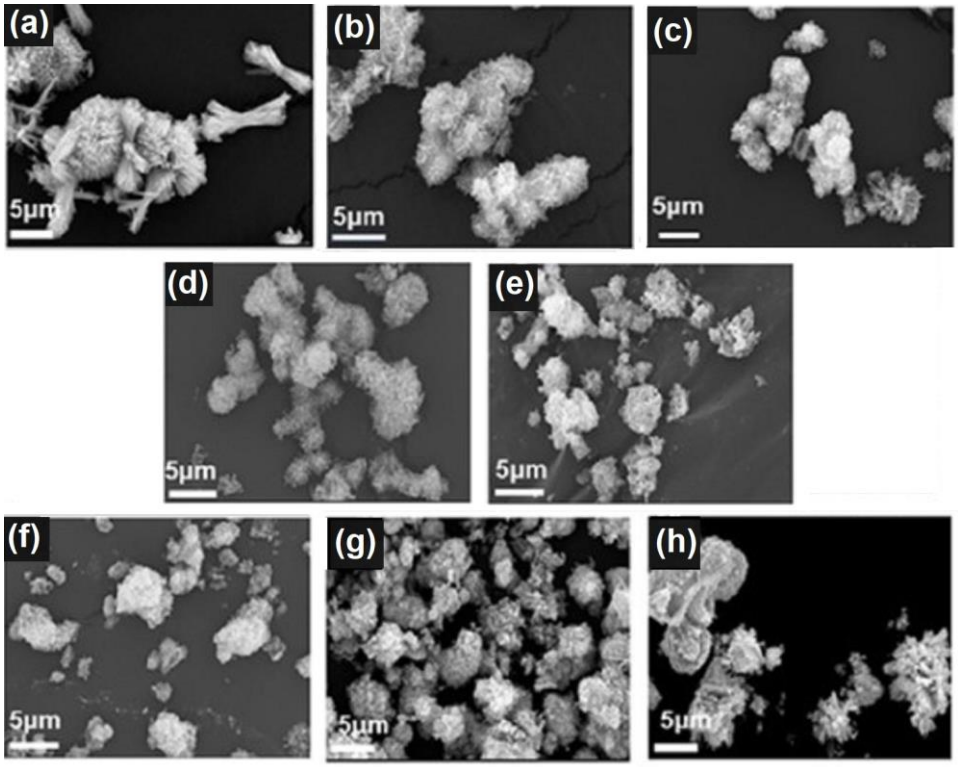

Figure 2. SEM images of the as-prepared samples (**a**) $Ni_{1.0}Co_{2.1}(S_{0.9}O_{0.1})_4$, (**b**) $Fe_{0.1}Ni_{1.4}Co_{2.9}(S_{0.87}O_{0.13})_4$, (**c**) $Fe_{0.2}Ni_{1.5}Co_{2.8}(S_{0.9}O_{0.1})_4$, (**d**) $Fe_{0.3}Ni_{1.2}Co_{2.5}(S_{0.9}O_{0.1})_4$, (**e**) $Fe_{0.6}Ni_{1.2}Co_{2.5}(S_{0.83}O_{0.17})_4$, (**f**) $Fe_{0.5}Ni_{1.0}Co_{2.0}(S_{0.57}Se_{0.25}O_{0.18})_4$, (**g**) $Fe_{0.4}Ni_{0.7}Co_{1.6}(Se_{0.81}O_{0.19})_4$, (**h**) $Ni_{0.7}Co_{1.4}(Se_{0.85}O_{0.15})_4$.

To further investigate the sulfoselenide $Fe_{0.5}Ni_{1.0}Co_{2.0}(S_{0.57}Se_{0.25}O_{0.18})_4$, transition electron microscopy, TEM-EDX, was performed. The TEM images, Figure 3, confirmed the needle-like microstructure. EDX-mapping also proved the uniform presence of Fe, Ni, Co, S, and Se in the sulfoselenide sample (see Supplementary Materials, Table S1 for atom ratios).

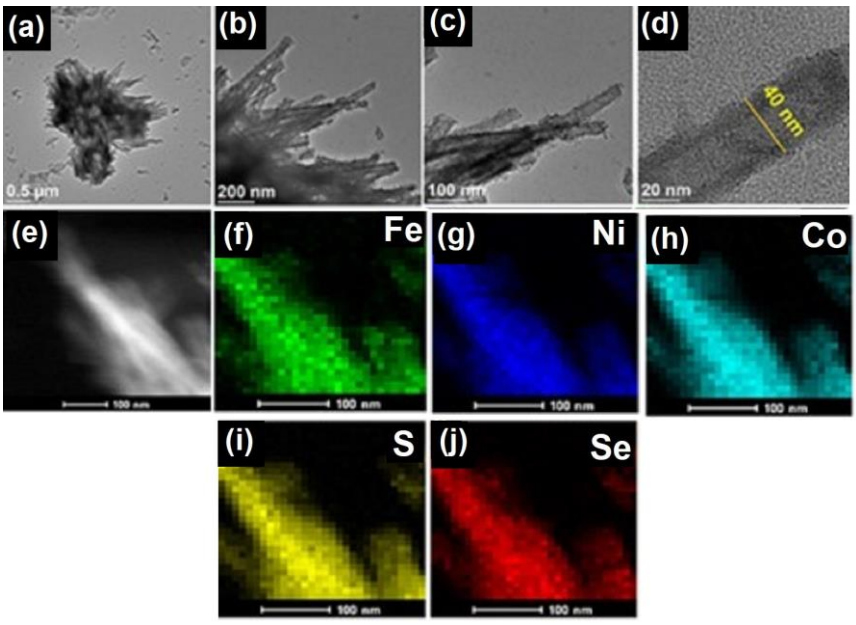

Figure 3. TEM images **(a-e)** of $Fe_{0.5}Ni_{1.0}Co_{2.0}(S_{0.57}Se_{0.25}O_{0.18})_4$ and **(f-j)** HAADF STEM-EDX mapping results of Fe, Ni, Co, S and Se, recorded from a nano needle section **(e)** of $Fe_{0.5}Ni_{1.0}Co_{2.0}(S_{0.57}Se_{0.25}O_{0.18})_4$.

Preprints (www.preprints.org) | NOT PEER-REVIEWED | Posted: 13 June 2023 doi:10.20944/preprints202306.0928.v1

Nitrogen adsorption-desorption isotherms, and specific surface area (BET) of the samples are given in Figure S10 and Table S7.

X-ray photoelectron spectroscopy (XPS) was conducted to determine the valence state of the elements in $Ni_{1.0}Co_{2.1}(S_{0.9}O_{0.1})_4$ and $Fe_{0.5}Ni_{1.0}Co_{2.0}(S_{0.57}Se_{0.25}O_{0.18})_4$. As shown in Figure S11, X-ray survey spectra indicate the existence of Ni, Co, and S in $Ni_{1.0}Co_{2.1}(S_{0.9}O_{0.1})_4$ and of Fe, Ni, Co, S, and Se in $Fe_{0.5}Ni_{1.0}Co_{2.0}(S_{0.57}Se_{0.25}O_{0.18})_4$. The high-resolution spectra of the metal atoms and of Se are shown in Figure 4, those of S 2p and O1s of $Ni_{1.0}Co_{2.1}(S_{0.9}O_{0.1})_4$ in Figure S12a and Figure S13a, respectively. The positions of the XPS peaks are summarized in Table S8 and S9. It should be noted that the analysis depth of XPS is only 0.7-11 nm as the detected photoelectrons can only escape from such a thin surface layer of the sample.

The metal ratios and the ratios between different oxidation states of nickel and cobalt (Table 1) were calculated by integrating the fitted peak area for each metal valence state using the Ni $2p_{3/2}$ and Co $2p_{3/2}$ regions. In $Ni_{1.0}Co_{2.1}(S_{0.9}O_{0.1})_4$ Ni^{2+} and Co^{3+} are the prevalent oxidation states.

Table 1. The metal ratios and the ratios between different oxidation states of nickel and cobalt in $Ni_{1.0}Co_{2.1}(S_{0.9}O_{0.1})_4$ and $Fe_{0.5}Ni_{1.0}Co_{2.0}(S_{0.57}Se_{0.25}O_{0.18})_4$.

Sample		At% [a]	Ni/Co [a]		At% [b]	Position (eV)	M^{2+}/M^{3+}
$Ni_{1.0}Co_{2.1}(S_{0.9}O_{0.1})_4$ [c]	Ni	6.90	1/2	Ni^{2+}	35.6	853.3	2.59
				Ni^{3+}	13.7	856.0	
	Co	13.90		Co^{2+}	17.0	780.3	0.37
				Co^{3+}	45.9	778.7	
			Fe/Ni/Co				
$Fe_{0.5}Ni_{1.0}Co_{2.0}(S_{0.57}Se_{0.25}O_{0.18})_4$ [d]	Fe	2.30	1.0/2.5/4.1				
	Ni	5.70		Ni^{2+}	3.3	854.5	0.10
				Ni^{3+}	32.9	856.5	
	Co	9.40		Co^{2+}	46.7	781.9	6.65
				Co^{3+}	7.0	779.1	

[a] From XPS survey spectrum (Figure S11, Suppl. Mater.). [b] Based on the Ni $2p_{3/2}$ and Co $2p_{3/2}$ regions in XPS. [c] Element composition from AAS-CHNS. [d] Element composition from AAS-CHNS-EDX(Se) (Tables S3-S6, Suppl. Mater.)

Based on element ratios obtained from AAS and CHNS analysis and also the metal valence states for nickel and cobalt in the $Ni_{1.0}Co_{2.1}(S_{0.9}O_{0.1})_4$ sample, the chemical formula can be given as $((Ni^{2+})_{0.72}(Ni^{3+})_{0.28})_{1.0}((Co^{2+})_{0.27}(Co^{3+})_{0.72})_{2.1}(S_{0.9}O_{0.1})_4$ which is anion-cation charge-balanced within rounding errors.

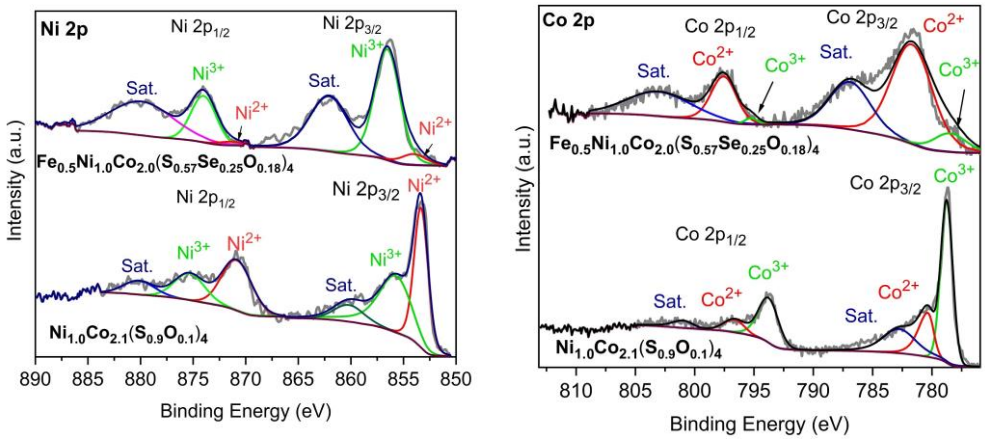

(a) **(b)**

Preprints (www.preprints.org) | NOT PEER-REVIEWED | Posted: 13 June 2023 doi:10.20944/preprints202306.0928.v1

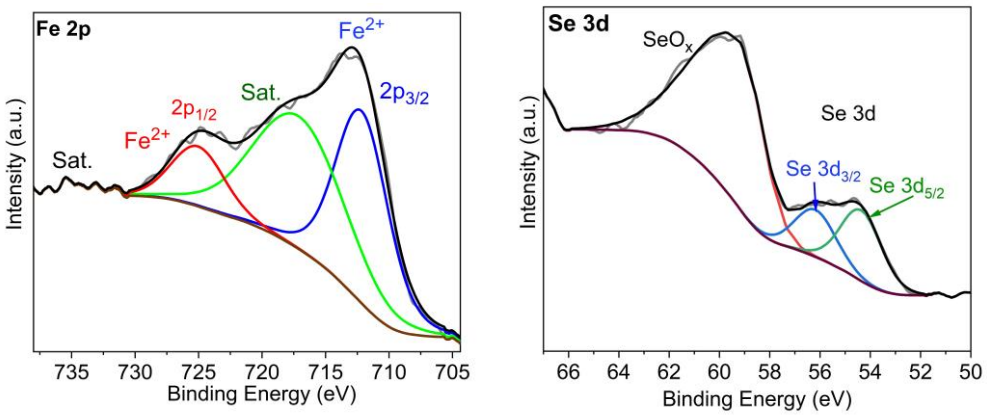

Figure 4. High-resolution XPS spectra of (**a**) Ni 2p region and (**b**) Co 2p region of $Ni_{1.0}Co_{2.1}(S_{0.9}O_{0.1})_4$ and $Fe_{0.5}Ni_{1.0}Co_{2.0}(S_{0.57}Se_{0.25}O_{0.18})_4$, (**c**) Fe 2p region and (**d**) Se 3d region of $Fe_{0.5}Ni_{1.0}Co_{2.0}(S_{0.57}Se_{0.25}O_{0.18})_4$.

In contrast to the $Ni_{1.0}Co_{2.1}(S_{0.9}O_{0.1})_4$ sample, Ni^{3+} and Co^{2+} are the dominant valence states in $Fe_{0.5}Ni_{1.0}Co_{2.0}(S_{0.57}Se_{0.25}O_{0.18})_4$, which might be one of the reasons for having an improved the OER performance of this catalyst. It is believed that Ni^{3+} can improve electrophilicity and oxygen adsorption, which can increase the amount of NiOOH active sites during the OER reaction [53].

The Fe 2p spectrum (Figure 4c) for $Fe_{0.5}Ni_{1.0}Co_{2.0}(S_{0.57}Se_{0.25}O_{0.18})_4$ represents two broad peaks at 712.5 eV and 725.0 eV, which can be assigned to Fe $2p_{3/2}$ and Fe $2p_{1/2}$, respectively [54]. Furthermore, two satellite peaks were detected at 717.5 and 734.5 eV [55,56]. The $2p_{3/2}$ spectrum range is 710 to 720 eV including the satellite peak, while the $2p_{1/2}$ spectrum range is 720–735 eV with the satellite peak. For iron it should be noted that the Fe 2p spectral background has a contribution from a Co_{LMM} and Ni_{LMM} Auger peaks, making an unequivocal deconvolution and peak assignment difficult [57,58]. The Se 3d XPS spectra of $Fe_{0.5}Ni_{1.0}Co_{2.0}(S_{0.57}Se_{0.25}O_{0.18})_4$ (Figure 4d) consist of two peaks centered at 55.0 and 57.0 eV, representing Se $3d_{5/2}$, and Se $3d_{3/2}$, respectively. The peak at 59.5 eV was attributed to SeO_x, forming on the surface due to exposure to air, and to the overlap with the Co 3p signal [39]. The high-resolution spectrum of S 2p and O 1s of $Fe_{0.5}Ni_{1.0}Co_{2.0}(S_{0.57}Se_{0.25}O_{0.18})_4$ are shown in Figure S12b and Figure 13b (Suppl. Mater.), respectively. Based on the elemental ratios obtained from AAS, CHNS and EDX(Se) analysis and also metal valence states for iron, nickel and cobalt in the $Fe_{0.5}Ni_{1.0}Co_{2.0}(S_{0.57}Se_{0.25}O_{0.18})_4$ sample the chemical formula can be given as $(Fe^{2+})_{0.5}((Ni^{2+})_{0.1}(Ni^{3+})_{0.9})_{1.0}((Co^{2+})_{0.87}(Co^{3+})_{0.13})_{2.0}(S_{0.57}Se_{0.25}O_{0.18})_4$.

3.3 Oxygen evolution reaction performance

The OER activity of the mixed-metal sulfides, selenides, and the sulfoselenide was evaluated by a three-electrode setup in 1.0 mol L^{-1} KOH solution. The working electrode was prepared according to a method used by Li et al.[29], a slurry containing 8:1:1 mass portions of the active materials (mixed-metal sulfide, selenide, or sulfoselenide material), carbon black, Vulcan XC-72R, and polyvinylidene fluoride, PVDF, respectively, in *N*-methyl-2-pyrrolidone, NMP (further details in experimental section). As is shown in Figure 6a, polarization curves of the as-prepared electrodes revealed that the presence of iron could reduce the overpotential of the $Ni_{1.0}Co_{2.1}(S_{0.9}O_{0.1})_4$ parent compound. In the polarization curves, the peaks around 1.3–1.4 eV are attributed to the oxidation of Ni^{2+}/Ni^{3+} [59].

The overpotential for $Ni_{1.0}Co_{2.1}(S_{0.9}O_{0.1})_4$ of 346 mV at 50 mA cm^{-2} was reduced with increasing iron content in $Fe_{0.1}Ni_{1.4}Co_{2.9}(S_{0.87}O_{0.13})_4$, $Fe_{0.2}Ni_{1.5}Co_{2.8}(S_{0.9}O_{0.1})_4$, $Fe_{0.3}Ni_{1.2}Co_{2.5}(S_{0.9}O_{0.1})_4$, and $Fe_{0.6}Ni_{1.2}Co_{2.5}(S_{0.83}O_{0.17})_4$ to 318, 310, 294, and 294 mV, respectively (Figure 5a,b). The electronic interaction between Fe, Ni, and Co in the iron-containing samples alters the electronic structure, making Ni^{2+} oxidation more difficult, resulting in a positive shift in the Ni^{2+}/Ni^{3+} anodic peak at 1.3–1.4 eV [30,37]. The reduction of the

Preprints (www.preprints.org) | NOT PEER-REVIEWED | Posted: 13 June 2023 doi:10.20944/preprints202306.0928.v1

OER overpotential in iron-containing samples can be attributed to reducing the charge transfer resistance through the synergistic electronic interaction between Fe, Co and Ni from a charge redistribution between active sites within the samples. Density functional theory (DFT) calculations in the literature traced the synergy to a decrease in the Gibbs free energy for the formation of a MOOH intermediate, which not only enhanced the intrinsic OER activity, but also significantly improved the intrinsic conductivity of iron-containing samples, greatly facilitating the charge transfer process [41,60].

In the next step, the effect of the coexistence of sulfur and selenium was investigated. The overpotential of $Fe_{0.5}Ni_{1.0}Co_{2.0}(S_{0.57}Se_{0.25}O_{0.18})_4$ (green line)of 277 mV at 50 mA cm^{-2} presents a 17 mV and 22 mV reduction compared to $Fe_{0.6}Ni_{1.2}Co_{2.5}(S_{0.83}O_{0.17})_4$ (294 mV) and RuO_2 (299 mV) (Figure 5c,d), indicating that the insertion of selenium improves the performance of the transition metal sulfide. Moreover, the OER performance of $Fe_{0.5}Ni_{1.0}Co_{2.0}(S_{0.57}Se_{0.25}O_{0.18})_4$ at 100 mA cm^{-2} only needed 299 mV while RuO_2 required 341 mV overpotential, which demonstrates the excellent electrocatalytic activity of $Fe_{0.5}Ni_{1.0}Co_{2.0}(S_{0.57}Se_{0.25}O_{0.18})_4$ even under a high current density. The boost of the OER activity of $Fe_{0.5}Ni_{1.0}Co_{2.0}(S_{0.57}Se_{0.25}O_{0.18})_4$ can be attributed to the effect of selenide incorporation that reduces the energy barrier of the OER reaction, optimizes the electronic structure of active sites via modulating of the d-band of the compound, and also accelerates the kinetics of the reaction [61].

Preprints (www.preprints.org) | NOT PEER-REVIEWED | Posted: 13 June 2023 doi:10.20944/preprints202306.0928.v1

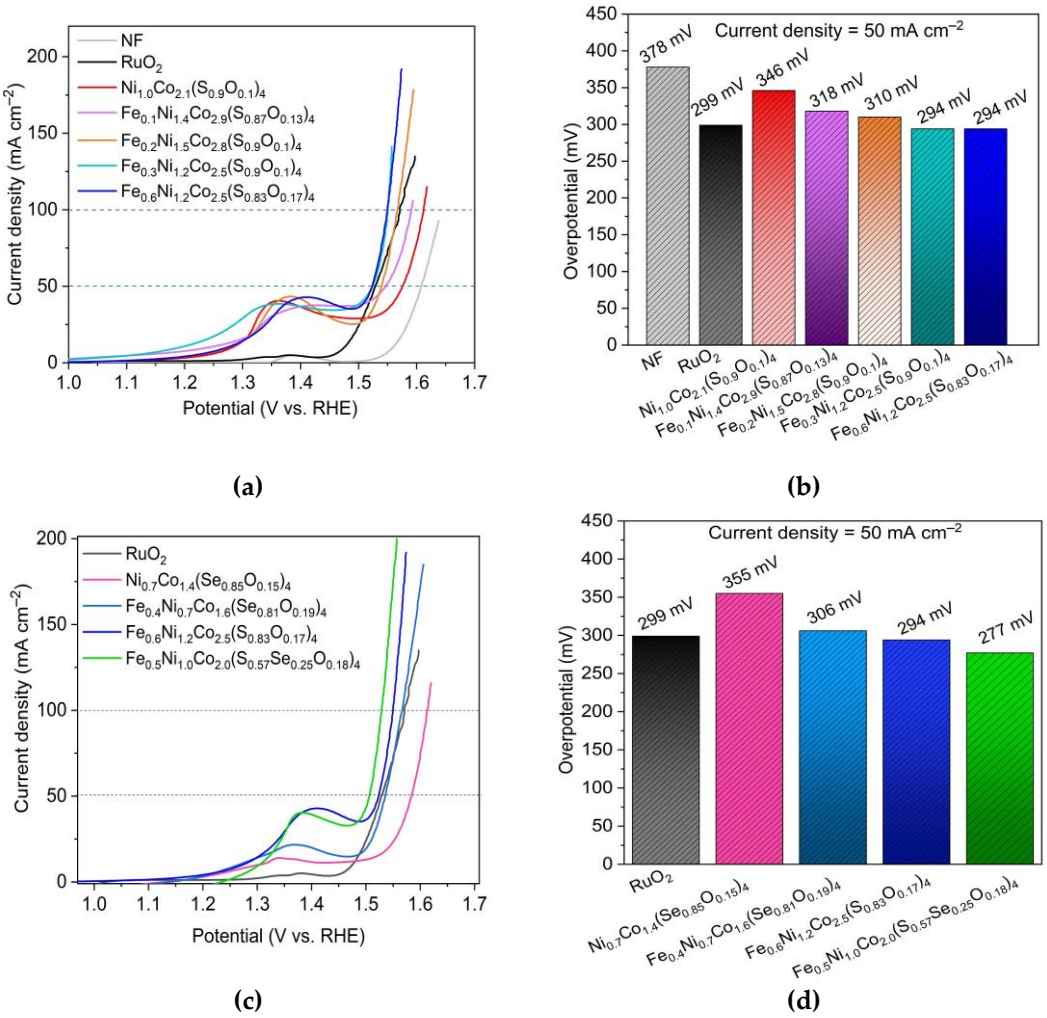

Figure 5. (**a**) OER LSV polarization curves and (**b**) bar chart of corresponding overpotentials at 50 mA cm^{-2} of iron-containing sulfides. (**c**) OER LSV polarization curves and (**d**) bar chart of corresponding overpotentials at 50 mA cm^{-2} of different iron-containing sulfides, selenides, and sulfoselenide .

The Tafel slopes of the samples were obtained from LSV polarization curves at a scan rate of 5 mV s^{-1} using the Tafel equation (1) [62]:

$$\eta = a + b \times \log(j) \quad (1)$$

η is the overpotential, b is the Tafel slope, j is the current density, and c is the intercept with the y-axis. The value of the Tafel slope is one of the most useful kinetic parameters and is inversely proportional to the kinetics of the OER reaction. Hence, as demonstrated in Figures 6a,b, $Fe_{0.5}Ni_{1.0}Co_{2.0}(S_{0.57}Se_{0.25}O_{0.18})_4$ with the lowest value of the Tafel slope presents the most favorable OER kinetics among the investigated samples. Besides, according to Krasil'shchikov's mechanistic paths (equation 2–5, M = active site, b = Tafel slope) [62,63] with their corresponding Tafel slope values, the rate-determining step of the OER reaction for $Ni_{1.0}Co_{2.1}(S_{0.9}O_{0.1})_4$ (b = 132 mV dec^{-1}) is metal oxidation with hydroxide formation (reaction (2)). By increasing the iron content in the samples, the Tafel slope decreased and reached 87 mV dec^{-1} for $Fe_{0.6}Ni_{1.2}Co_{2.5}(S_{0.83}O_{0.17})_4$, suggesting that metal oxidation with hydroxide formation (2) and deprotonation of a metal hydroxide (3) both present rate-determining steps.

The lowest Tafel slope among the samples belongs to the sulfoselenide $Fe_{0.5}Ni_{1.0}Co_{2.0}(S_{0.57}Se_{0.25}O_{0.18})_4$ with 75 mV dec^{-1}, which is again evidence for the role of selenium in enhancing the kinetics of the OER reaction. The Tafel value of 75 mV dec^{-1} of

Preprints (www.preprints.org) | NOT PEER-REVIEWED | Posted: 13 June 2023 doi:10.20944/preprints202306.0928.v1

$Fe_{0.5}Ni_{1.0}Co_{2.0}(S_{0.57}Se_{0.25}O_{0.18})_4$ is close to reaction (3) (b = 60 mV dec^{-1}) being then rate-determining in the overall OER process.

$$M + OH^- \leftrightarrows MOH + e^-,\ b = 120\ mV\ dec^{-1} \quad (2)$$

$$MOH + OH^- \leftrightarrows MO^- + H_2O,\ b = 60\ mV\ dec^{-1} \quad (3)$$

$$MO^- \rightarrow MO + e^-,\ b = 45\ mV\ dec^{-1} \quad (4)$$

$$2MO \rightarrow 2M + O_2,\ b = 19\ mV\ dec^{-1} \quad (5)$$

Electrochemical impedance spectroscopy (EIS) was conducted for the electron-transfer kinetics during the OER reaction and to justify the obtained overpotentials [64]. Figure 6c shows Nyquist plots of the samples at the potential of 1.5 V vs. RHE. The semicircle diameter of Nyquist plots is inversely proportional to the charge transfer rate across the electrode and the electrolyte that accelerates reaction kinetics. Hence, a smaller semicircle diameter represents more favorable charge transfer kinetics [24].

The smaller semicircle diameter of the $Fe_{0.5}Ni_{1.0}Co_{2.0}(S_{0.57}Se_{0.25}O_{0.18})_4$ Nyquist plot indicates that the coexistence of iron and selenium in $Fe_{0.5}Ni_{1.0}Co_{2.0}(S_{0.57}Se_{0.25}O_{0.18})_4$ can reduce the charge transfer resistance (Rct). Furthermore, a Voigt circuit model was applied to the Nyquist plots to evaluate the specific value for the charge resistance in the OER process. As shown in Table 2, the value of charge resistance for $Fe_{0.5}Ni_{1.0}Co_{2.0}(S_{0.57}Se_{0.25}O_{0.18})_4$ is the lowest (0.8 Ω) compared to the other investigated samples. The results from the Rct values are in line with the recorded OER overpotentials of the samples and the electrocatalytic performance.

To elucidate the importance of sulfur and selenium in the OER electrocatalysis performance, the $(Fe_xNi_{1-x})CoCH$-(1.0) precursor for $Fe_{0.6}Ni_{1.2}Co_{2.5}(S_{0.83}O_{0.17})_4$ and $Fe_{0.5}Ni_{1.0}Co_{2.0}(S_{0.57}Se_{0.25}O_{0.18})_4$ was investigated and found to have an OER LSV polarization curve with a higher overpotential of 330 mV vs. RHE to reach 50 mA cm^{-2} and a Tafel slope of 98 mV dec^{-1}, higher than the iron-containing sulfide and sulfoselenide (Table 2, Figure S14). Furthermore, the larger Nyquist plot semicircle diameter and higher charge transfer resistance (R_{ct} = 2.5 Ω) of $(Fe_xNi_{1-x})CoCH$-(1.0) imply the importance of S and Se in facilitating the charge transfer through the electrode-electrolyte interface in sulfide, selenides, and sulfoselenide samples (Figure S15).

Table 2. Overpotential at 50 mA cm^{-2}, Tafel slopes, and estimated charge transfer resistance of selected samples at 1.5 V vs. RHE.

Sample	Overpotential (mV)	Tafel slope (mV dec^{-1})	Charge transfer resistant Rct (Ω)
$Ni_{1.0}Co_{2.1}(S_{0.9}O_{0.1})_4$	346	132	1.8
$Ni_{0.7}Co_{1.4}(Se_{0.85}O_{0.15})$	355	135	1.7
$Fe_{0.6}Ni_{1.2}Co_{2.5}(S_{0.83}O_{0.17})_4$	294	87	2.2
$Fe_{0.4}Ni_{0.7}Co_{1.6}(Se_{0.81}O_{0.19})_4$	306	84	1.4
$Fe_{0.5}Ni_{1.0}Co_{2.0}(S_{0.57}Se_{0.25}O_{0.18})_4$	277	75	0.8
$(Fe_xNi_{1-x})CoCH$-(1.0)	330	98	2.5
RuO_2	299	66	1.2

One of the critical parameters to evaluate the performance of electrocatalysts in practical applications is their long-term stability. Hence, a chronopotentiometry test at a current density of 50 mA cm^{-2} for 20 h was conducted to evaluate the long-term stability performance of the $Fe_{0.5}Ni_{1.0}Co_{2.0}(S_{0.57}Se_{0.25}O_{0.18})_4$ [47].

Figure 6d illustrates that after 20 h of OER reaction, the overpotential for obtaining 50 mA cm^{-2} increased only from 277 mV to 279 mV, which is essentially constant and supports the excellent electrocatalyst stability of $Fe_{0.5}Ni_{1.0}Co_{2.0}(S_{0.57}Se_{0.25}O_{0.18})_4$ for practical applications. The more so as for RuO_2 the overpotential increases from 300 mV to 375 mV at the same chronopotentiometry test for 20 h, at 50 mA cm^{-2}. A recent study by Jiang et al.

Preprints (www.preprints.org) | NOT PEER-REVIEWED | Posted: 13 June 2023 doi:10.20944/preprints202306.0928.v1

[65] proved that a SeO_x film on the surface could improve the catalyst stability in the OER reaction, which can be the reason behind the high stability of $Fe_{0.5}Ni_{1.0}Co_{2.0}(S_{0.57}Se_{0.25}O_{0.18})_4$ during the OER reaction (the overpotential increased from 277 to only 279 at 50 mA cm^{-1} after 20 h OER reaction).

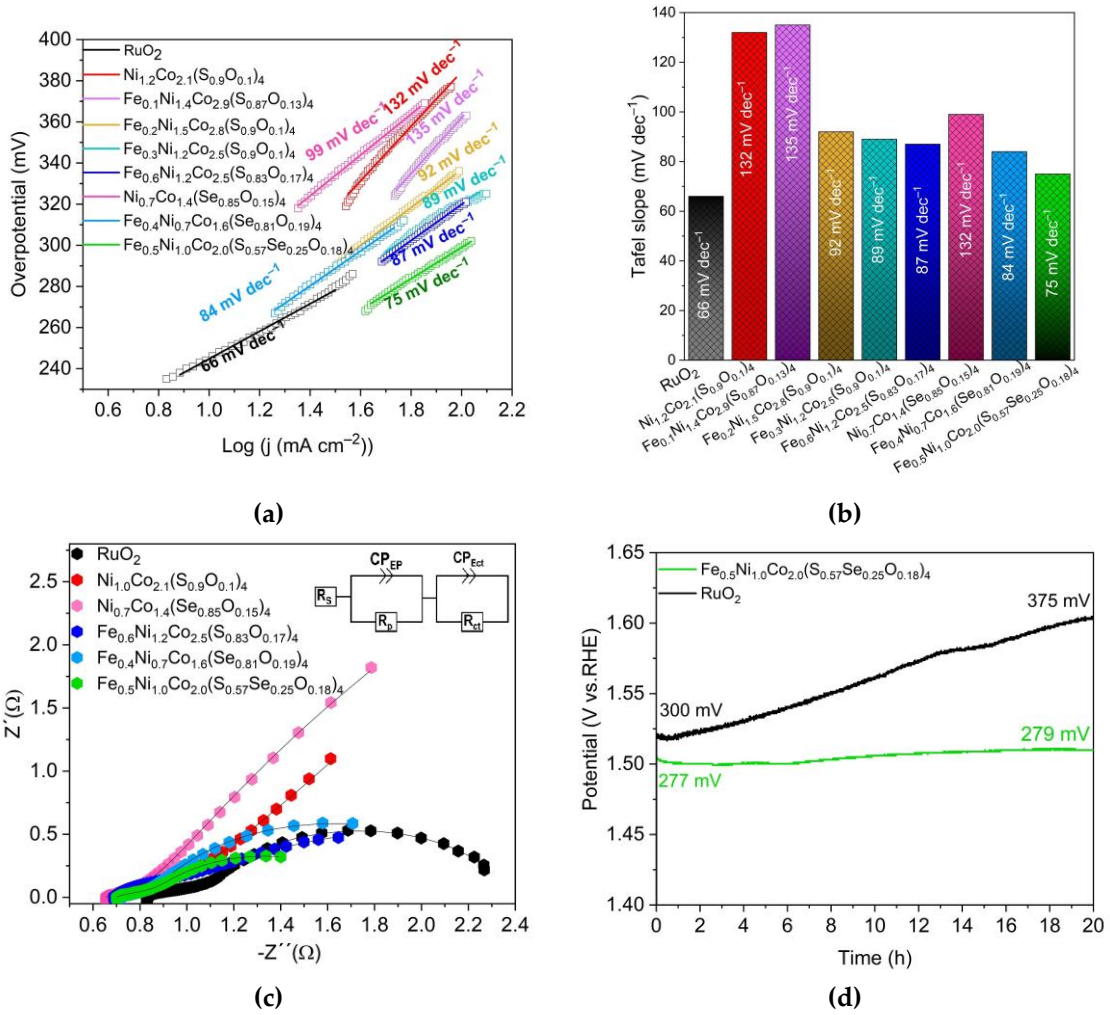

Figure 6. (**a**) Tafel plots and (**b**) bar chart of Tafel slopes of the samples. (**c**) Nyquist plots of selected samples and Voigt circuit model. (**d**) Chronopotentiometry test of $Fe_{0.5}Ni_{1.0}Co_{2.0}(S_{0.57}Se_{0.25}O_{0.18})_4$ and RuO_2.

The superior OER activity and stability of $Fe_{0.5}Ni_{1.0}Co_{2.0}(S_{0.57}Se_{0.25}O_{0.18})_4$ material can be attributed to several effects resulting from introducing Fe and Se^{2-} in the structure of the nickel cobalt sulfide base material: Introducing Fe sites can enhance OER performance a) by optimizing bond energies for OER intermediates adsorbing on the electrode surface, which facilitates the OER kinetics [66], b) by overcoming the metal oxidation step and facilitating O_2 evolution [67], c) by improving the conductivity of the electrode film [68].

For comparison, the overpotential values of several high performance electrocatalysts at a current density of 50 mA cm^{-2} using nickel foam as substrate are presented in Table 3. Notably, the results demonstrate that the OER performance of the sulfoselenide $Fe_{0.5}Ni_{1.0}Co_{2.0}(S_{0.57}Se_{0.25}O_{0.18})_4$ is on par with the best electrocatalysts reported in the literature, highlighting its comparable effectiveness.

Table 3. Comparison of nickel- and cobalt-based electrocatalysts for OER.

Preprints (www.preprints.org) | NOT PEER-REVIEWED | Posted: 13 June 2023 doi:10.20944/preprints202306.0928.v1

Catalyst	Overpotential (mV)	Current density (mA cm^{-2})	Electrode substrate[a)]	Ref.
$Fe_{0.5}Ni_{1.0}Co_{2.0}(S_{0.57}Se_{0.25}O_{0.18})_4$	277	50	NF	This work
$Co_3O_4/NiCo_2O_4$	407	50	NF	[69]
NiO/α-Fe_2O_3	244	50	NF	[70]
P-$Ni_3S_2/CoFe_2O_4$	254	50	NF	[71]
PANI[b)]/NiFe–OH	260	50	NF	[72]
$LaCoO_3$	420	50	NF	[73]
Ce-doped Ni_3S_2	257	50	NF	[74]
Porous Ni_3S_2	291	50	NF	[75]
$(Co_{1.2}MoO_{4.21}\cdot 3H_2O)/Ni_3S_2$	290	50	NF	[76]
$CoHPO_4\cdot H_2O$	350	50	NF	[77]
NiSe@NiOOH	300	50	NF	[78]
P-containing $NiCo_2S_4$	300	50	NF	[38]
NiFe-LDH[c)]/Co_3O_4	274	50	NF	[79]

[b)] NF = nickel foam; as we used a nickel foam electrode and current denities of 50 mA cm^{-2} this comparative listing is restricted to the same conditions. [b)] PANI = polyaniline. [c)] LDH = layered double hydroxides.

4. Conclusions

A novel trimetallic sulfoselenide, $Fe_{0.5}Ni_{1.0}Co_{2.0}(S_{0.57}Se_{0.25}O_{0.18})_4$, electrocatalyst was synthesized via two steps hydrothermal method. The mixed-metal sulfoselenide possessed high OER activity than to the bimetallic nickel cobalt sulfide $Ni_{1.0}Co_{2.1}(S_{0.9}O_{0.1})_4$, the bimetallic nickel cobalt selenide $Ni_{0.7}Co_{1.4}(Se_{0.85}O_{0.15})_4$, the trimetallic iron-containing nickel cobalt sulfides, $Fe_{0.1}Ni_{1.4}Co_{2.9}(S_{0.87}O_{0.13})_4$, $Fe_{0.2}Ni_{1.5}Co_{2.8}(S_{0.9}O_{0.1})_4$, $Fe_{0.3}Ni_{1.2}Co_{2.5}(S_{0.9}O_{0.1})_4$, and $Fe_{0.6}Ni_{1.2}Co_{2.5}(S_{0.83}O_{0.17})_4$ and the iron-containing nickel cobalt selenide $Fe_{0.4}Ni_{0.7}Co_{1.6}(Se_{0.81}O_{0.19})_4$. The trimetallic sulfoselenide required an overpotential of only 277 mV at 50 mV cm^{-2} and had favorable OER kinetics, manifested by a Tafel slope of 75 mV dec^{-1}. The OER performance of $Fe_{0.5}Ni_{1.0}Co_{2.0}(S_{0.57}Se_{0.25}O_{0.18})_4$ surpassed the well-known RuO_2 benchmark material where the required overpotential (300 mV to generate 50 mA cm^{-2}) was 23 mV higher at the same condition (1 mol L^{-1} KOH). The 20 h chronopotentiometry analysis revealed that $Fe_{0.5}Ni_{1.0}Co_{2.0}(S_{0.57}Se_{0.25}O_{0.18})_4$ has remarkable stability during long-term operation in alkaline media (the overpotential increased only from 277 to 279 mV) while at the same condition, RuO_2 showed a considerable loss in activity (such that the overpotential increased from 300 to 375 mV during the generation of 50 mA cm^{-2} current density).

Furthermore, the incorporation of selenium also significantly affected the OER activity and stability by reducing the energy barrier of the OER reaction, optimizing the electronic structure of active sites by modifying the d-band of the materials. Indeed, a SeO_x film on the surface of $Fe_{0.5}Ni_{1.0}Co_{2.0}(S_{0.57}Se_{0.25}O_{0.18})_4$ can enhance the long-term stability of the catalyst. Considering the improvements in OER performance, this simple two-step hydrothermal synthesis of trimetallic sulfoselenides, from transition metal carbonate hydroxide, $(Fe_xNi_{1-x})CoCH$-(y) as precursors can be used as a facile and practical approach to produce the next generation of non-precious polymetallic polychalcogenide materials for the oxygen evolution reaction.

Supplementary Materials: The following supporting information can be downloaded at: www.mdpi.com/xxx/ Section S1: preparation of $Ni_{0.7}Co_{1.4}(Se_{0.85}O_{0.15})_4$ and $Ni_{1.0}Co_{2.1}(S_{0.9}O_{0.1})_4$; Section S2: Sample preparation for AAS; Section S3: Scanning electron microscopy and energy dispersive X-ray spectroscopy (SEM/EDX) and TEM/EDX; Section S4: Elemental analysis and atomic spectroscopy measurements; Section S5: Nitrogen sorption measurement; Section S6: X-ray photoelectron spectroscopy; Section S7: Electrochemical characterization; References [80–94] are cited in the Supplementary Materials.

Author Contributions: Conceptualization: S.A and C.J; methodology: S.A; validation: S.A; formal analysis: S.A, L.A, M.F and T.H.Y.B; writing—original draft preparation: S.A; writing—review and editing: S.A and C.J; Supervision: C.J; project administration: C.J; funding acquisition: C.J

Funding: This research was funded by a joint National Natural Science Foundation of China–Deutsche Forschungsgemeinschaft (NSFC-DFG) project (DFG JA466/39-1).

Institutional Review Board Statement: Not applicable.

Informed Consent Statement: Not applicable.

Data Availability Statement: The data presented in this study are available on request from the corresponding author.

Acknowledgments: The authors also thank Annette Ricken for the AAS measurements.

Conflicts of Interest: The authors declare no conflict of interest.

Sample Availability: Samples of the compounds will not be available.

References

1. Conti, J.; Holtberg, P.; Diefenderfer, J.; LaRose, A.; Turnure, J.T.; Westfall, L. *International Energy Outlook 2016 With Projections to 2040*; 2016; p. DOE/EIA--0484(2016), 1296780;
2. Wu, D.; Kusada, K.; Yoshioka, S.; Yamamoto, T.; Toriyama, T.; Matsumura, S.; Chen, Y.; Seo, O.; Kim, J.; Song, C.; et al. Efficient Overall Water Splitting in Acid with Anisotropic Metal Nanosheets. *Nat. Commun.* **2021**, *12*, 1145, doi:10.1038/s41467-021-20956-4.
3. Huang, W.; Zhang, J.; Liu, D.; Xu, W.; Wang, Y.; Yao, J.; Tan, H.T.; Dinh, K.N.; Wu, C.; Kuang, M.; et al. Tuning the Electronic Structures of Multimetal Oxide Nanoplates to Realize Favorable Adsorption Energies of Oxygenated Intermediates. *ACS Nano* **2020**, *14*, 17640–17651, doi:10.1021/acsnano.0c08571.
4. Jiao, Y.; Zheng, Y.; Jaroniec, M.; Qiao, S.Z. Design of Electrocatalysts for Oxygen- and Hydrogen-Involving Energy Conversion Reactions. *Chem. Soc. Rev.* **2015**, *44*, 2060–2086, doi:10.1039/C4CS00470A.
5. Du, P.; Eisenberg, R. Catalysts Made of Earth-Abundant Elements (Co, Ni, Fe) for Water Splitting: Recent Progress and Future Challenges. *Energy Environ. Sci.* **2012**, *5*, 6012, doi:10.1039/c2ee03250c.
6. Yu, Y.; Li, P.; Wang, X.; Gao, W.; Shen, Z.; Zhu, Y.; Yang, S.; Song, W.; Ding, K. Vanadium Nanobelts Coated Nickel Foam 3D Bifunctional Electrode with Excellent Catalytic Activity and Stability for Water Electrolysis. *Nanoscale* **2016**, *8*, 10731–10738, doi:10.1039/C6NR02395A.
7. Sondermann, L.; Jiang, W.; Shviro, M.; Spieß, A.; Woschko, D.; Rademacher, L.; Janiak, C. Nickel-Based Metal-Organic Frameworks as Electrocatalysts for the Oxygen Evolution Reaction (OER). *Molecules* **2022**, *27*, 1241, doi:10.3390/molecules27041241.
8. Öztürk, S.; Moon, G.; Spieß, A.; Budiyanto, E.; Roitsch, S.; Tüysüz, H.; Janiak, C. A Highly-Efficient Oxygen Evolution Electrocatalyst Derived from a Metal-Organic Framework and Ketjenblack Carbon Material. *ChemPlusChem* **2021**, *86*, 1106–1115, doi:10.1002/cplu.202100278.
9. Wei, C.; Rao, R.R.; Peng, J.; Huang, B.; Stephens, I.E.L.; Risch, M.; Xu, Z.J.; Shao-Horn, Y. Recommended Practices and Benchmark Activity for Hydrogen and Oxygen Electrocatalysis in Water Splitting and Fuel Cells. *Adv. Mater.* **2019**, *31*, 1806296, doi:10.1002/adma.201806296.
10. Kong, D.; Cha, J.J.; Wang, H.; Lee, H.R.; Cui, Y. First-Row Transition Metal Dichalcogenide Catalysts for Hydrogen Evolution Reaction. *Energy Environ. Sci.* **2013**, *6*, 3553, doi:10.1039/c3ee42413h.
11. Qu, M.; Jiang, Y.; Yang, M.; Liu, S.; Guo, Q.; Shen, W.; Li, M.; He, R. Regulating Electron Density of NiFe-P Nanosheets Electrocatalysts by a Trifle of Ru for High-Efficient Overall Water Splitting. *Appl. Catal. B* **2020**, *263*, 118324, doi:10.1016/j.apcatb.2019.118324.
12. Jiang, F.; Choy, W.C.H.; Li, X.; Zhang, D.; Cheng, J. Post-Treatment-Free Solution-Processed Non-Stoichiometric NiO_x Nanoparticles for Efficient Hole-Transport Layers of Organic Optoelectronic Devices. *Adv. Mater.* **2015**, *27*, 2930–2937, doi:10.1002/adma.201405391.
13. Chen, Z.; Deng, W.; Li, D.; Gai, Y.; Xie, W.; Hu, X.; Han, S.; Xu, N.; Qiao, S.; Yu, J.; et al. Construction of CoNiSSe-g-C_3N_4 Nanosheets with High Exposed Conductive Interface for Boosting Oxygen Evolution Reaction. *J. Alloys Compd.* **2021**, *887*, 161346, doi:10.1016/j.jallcom.2021.161346.
14. Wang, N.; Cao, Z.; Kong, X.; Liang, J.; Zhang, Q.; Zheng, L.; Wei, C.; Chen, X.; Zhao, Y.; Cavallo, L.; et al. Activity Enhancement *via* Borate Incorporation into a NiFe (Oxy)Hydroxide Catalyst for Electrocatalytic Oxygen Evolution. *J. Mater. Chem. A* **2018**, *6*, 16959–16964, doi:10.1039/C8TA04762F.
15. Zhang, X.; Liang, Y. Nickel Hydr(Oxy)Oxide Nanoparticles on Metallic MoS_2 Nanosheets: A Synergistic Electrocatalyst for Hydrogen Evolution Reaction. *Adv. Sci.* **2018**, *5*, 1700644, doi:10.1002/advs.201700644.

16. Subbaraman, R.; Tripkovic, D.; Chang, K.-C.; Strmcnik, D.; Paulikas, A.P.; Hirunsit, P.; Chan, M.; Greeley, J.; Stamenkovic, V.; Markovic, N.M. Trends in Activity for the Water Electrolyser Reactions on 3d M(Ni,Co,Fe,Mn) Hydr(Oxy)Oxide Catalysts. *Nat. Mater* **2012**, *11*, 550–557, doi:10.1038/nmat3313.
17. Denny, S.R.; Tackett, B.M.; Tian, D.; Sasaki, K.; Chen, J.G. Exploring Electrocatalytic Stability and Activity of Unmodified and Platinum-Modified Tungsten and Niobium Nitrides. *Int. J. Hydrog. Energy* **2020**, *45*, 22883–22892, doi:10.1016/j.ijhydene.2020.06.186.
18. Wang, C.; Chen, W.; Yuan, D.; Qian, S.; Cai, D.; Jiang, J.; Zhang, S. Tailoring the Nanostructure and Electronic Configuration of Metal Phosphides for Efficient Electrocatalytic Oxygen Evolution Reactions. *Nano Energy* **2020**, *69*, 104453, doi:10.1016/j.nanoen.2020.104453.
19. Fu, G.; Lee, J.-M. Ternary Metal Sulfides for Electrocatalytic Energy Conversion. *J. Mater. Chem. A* **2019**, *7*, 9386–9405, doi:10.1039/C9TA01438A.
20. Chen, H.; Jiang, J.; Zhang, L.; Wan, H.; Qi, T.; Xia, D. Highly Conductive $NiCo_2S_4$ Urchin-like Nanostructures for High-Rate Pseudocapacitors. *Nanoscale* **2013**, *5*, 8879-8883, doi:10.1039/c3nr02958a.
21. Shen, L.; Yu, L.; Wu, H.B.; Yu, X.-Y.; Zhang, X.; Lou, X.W. Formation of Nickel Cobalt Sulfide Ball-in-Ball Hollow Spheres with Enhanced Electrochemical Pseudocapacitive Properties. *Nat. Commun* **2015**, *6*, 6694, doi:10.1038/ncomms7694.
22. Kulkarni, P.; Nataraj, S.K.; Balakrishna, R.G.; Nagaraju, D.H.; Reddy, M.V. Nanostructured Binary and Ternary Metal Sulfides: Synthesis Methods and Their Application in Energy Conversion and Storage Devices. *J. Mater. Chem. A* **2017**, *5*, 22040–22094, doi:10.1039/C7TA07329A.
23. Liu, W.; Zhang, J.; Bai, Z.; Jiang, G.; Li, M.; Feng, K.; Yang, L.; Ding, Y.; Yu, T.; Chen, Z.; et al. Controllable Urchin-Like $NiCo_2S_4$ Microsphere Synergized with Sulfur-Doped Graphene as Bifunctional Catalyst for Superior Rechargeable Zn-Air Battery. *Adv. Funct. Mater.* **2018**, *28*, 1706675, doi:10.1002/adfm.201706675.
24. Zhu, W.; Ren, M.; Hu, N.; Zhang, W.; Luo, Z.; Wang, R.; Wang, J.; Huang, L.; Suo, Y.; Wang, J. Traditional $NiCo_2S_4$ Phase with Porous Nanosheets Array Topology on Carbon Cloth: A Flexible, Versatile and Fabulous Electrocatalyst for Overall Water and Urea Electrolysis. *ACS. Sustain. Chem. Eng.* **2018**, *6*, 5011–5020, doi:10.1021/acssuschemeng.7b04663.
25. Feng, X.; Jiao, Q.; Liu, T.; Li, Q.; Yin, M.; Zhao, Y.; Li, H.; Feng, C.; Zhou, W. Facile Synthesis of Co_9S_8 Hollow Spheres as a High-Performance Electrocatalyst for the Oxygen Evolution Reaction. *ACS Sustain. Chem. Eng.* **2018**, *6*, 1863–1871, doi:10.1021/acssuschemeng.7b03236.
26. Chauhan, M.; Reddy, K.P.; Gopinath, C.S.; Deka, S. Copper Cobalt Sulfide Nanosheets Realizing a Promising Electrocatalytic Oxygen Evolution Reaction. *ACS Catal.* **2017**, *7*, 5871–5879, doi:10.1021/acscatal.7b01831.
27. Li, X.; Kou, Z.; Xi, S.; Zang, W.; Yang, T.; Zhang, L.; Wang, J. Porous $NiCo_2S_4$/FeOOH Nanowire Arrays with Rich Sulfide/Hydroxide Interfaces Enable High OER Activity. *Nano Energy* **2020**, *78*, 105230, doi:10.1016/j.nanoen.2020.105230.
28. Xu, X.; Liu, X.; Zhong, W.; Zhang, L.; Liu, G.; Du, Y. Nanostructured $NiCo_2S_4$@$NiCo_2O_4$-Reduced Graphene Oxide as an Efficient Hydrogen Evolution Electrocatalyst in Alkaline Electrolyte. *J. Colloid Interface Sci.* **2021**, *601*, 570–580, doi:10.1016/j.jcis.2021.05.148.
29. Li, H.; Chen, L.; Jin, P.; Li, Y.; Pang, J.; Hou, J.; Peng, S.; Wang, G.; Shi, Y. $NiCo_2S_4$ Microspheres Grown on N, S Co-Doped Reduced Graphene Oxide as an Efficient Bifunctional Electrocatalyst for Overall Water Splitting in Alkaline and Neutral PH. *Nano Res.* **2022**, *15*, 950–958, doi:10.1007/s12274-021-3580-z.
30. Liu, Q.; Jin, J.; Zhang, J. $NiCo_2S_4$@graphene as a Bifunctional Electrocatalyst for Oxygen Reduction and Evolution Reactions. *ACS Appl. Mater. Interfaces* **2013**, *5*, 5002–5008, doi:10.1021/am4007897.
31. Fereja, S.L.; Li, P.; Zhang, Z.; Guo, J.; Fang, Z.; Li, Z.; Chen, W. Construction of $NiCo_2S_4$/Fe_2O_3 Hybrid Nanostructure as a Highly Efficient Electrocatalyst for the Oxygen Evolution Reaction. *Electrochim. Acta* **2022**, *405*, 139793, doi:10.1016/j.electacta.2021.139793.
32. Liu, J.; Wang, J.; Zhang, B.; Ruan, Y.; Lv, L.; Ji, X.; Xu, K.; Miao, L.; Jiang, J. Hierarchical $NiCo_2S_4$@NiFe LDH Heterostructures Supported on Nickel Foam for Enhanced Overall-Water-Splitting Activity. *ACS Appl. Mater. Interfaces* **2017**, *9*, 15364–15372, doi:10.1021/acsami.7b00019.
33. Huang, Y.; Ge, S.; Chen, X.; Xiang, Z.; Zhang, X.; Zhang, R.; Cui, Y. Hierarchical $FeCo_2S_4$@$FeNi_2S_4$ Core/Shell Nanostructures on Ni Foam for High-Performance Supercapacitors. *Chem. Eur. J.* **2019**, *25*, 14117–14122, doi:10.1002/chem.201902868.
34. Govindasamy, M.; Shanthi, S.; Elaiyappillai, E.; Wang, S.-F.; Johnson, P.M.; Ikeda, H.; Hayakawa, Y.; Ponnusamy, S.; Muthamizhchelvan, C. Fabrication of Hierarchical $NiCo_2S_4$@CoS_2 Nanostructures on Highly Conductive Flexible Carbon Cloth Substrate as a Hybrid Electrode Material for Supercapacitors with Enhanced Electrochemical Performance. *Electrochim. Acta* **2019**, *293*, 328–337, doi:10.1016/j.electacta.2018.10.051.
35. Yu, X.; Xu, S.; Liu, X.; Cheng, X.; Du, Y.; Wu, Q. Mn-Doped $NiCo_2S_4$ Nanosheet Array as an Efficient and Durable Electrocatalyst for Oxygen Evolution Reaction. *J. Alloys Compd.* **2021**, *878*, 160388, doi:10.1016/j.jallcom.2021.160388.
36. Lai, F.; Feng, J.; Heil, T.; Tian, Z.; Schmidt, J.; Wang, G.-C.; Oschatz, M. Partially Delocalized Charge in Fe-Doped $NiCo_2S_4$ Nanosheet–Mesoporous Carbon-Composites for High-Voltage Supercapacitors. *J. Mater. Chem. A* **2019**, *7*, 19342–19347, doi:10.1039/C9TA06250E.
37. Wu, Y.; Liu, X.; Han, D.; Song, X.; Shi, L.; Song, Y.; Niu, S.; Xie, Y.; Cai, J.; Wu, S.; et al. Electron Density Modulation of $NiCo_2S_4$ Nanowires by Nitrogen Incorporation for Highly Efficient Hydrogen Evolution Catalysis. *Nat. Commun* **2018**, *9*, 1425, doi:10.1038/s41467-018-03858-w.

38. Min, K.; Yoo, R.; Kim, S.; Kim, H.; Shim, S.E.; Lim, D.; Baeck, S.-H. Facile Synthesis of P-Doped $NiCo_2S_4$ Nanoneedles Supported on Ni Foam as Highly Efficient Electrocatalysts for Alkaline Oxygen Evolution Reaction. *Electrochim. Acta* **2021**, *396*, 139236, doi:10.1016/j.electacta.2021.139236.
39. Liang, T.; Lenus, S.; Liu, Y.; Chen, Y.; Sakthivel, T.; Chen, F.; Ma, F.; Dai, Z. Interface and M^{3+}/M^{2+} Valence Dual-Engineering on Nickel Cobalt Sulfoselenide/Black Phosphorus Heterostructure for Efficient Water Splitting Electrocatalysis. *Energy Environ. Mater.* **2023**, *6*, doi:10.1002/eem2.12332.
40. Gong, Q.; Cheng, L.; Liu, C.; Zhang, M.; Feng, Q.; Ye, H.; Zeng, M.; Xie, L.; Liu, Z.; Li, Y. Ultrathin $MoS_{2(1-x)}Se_{2x}$ Alloy Nanoflakes For Electrocatalytic Hydrogen Evolution Reaction. *ACS Catal.* **2015**, *5*, 2213–2219, doi:10.1021/cs501970w.
41. Zhou, Y.; Wang, Y.; Zhao, H.; Su, J.; Zhang, H.; Wang, Y. Investigation of Anion Doping Effect to Boost Overall Water Splitting. *J. Catal.* **2020**, *381*, 84–95, doi:10.1016/j.jcat.2019.10.026.
42. Liu, R.; Xu, S.; Shao, X.; Wen, Y.; Shi, X.; Huang, L.; Hong, M.; Hu, J.; Yang, Z. Defect-Engineered NiCo-S Composite as a Bifunctional Electrode for High-Performance Supercapacitor and Electrocatalysis. *ACS Appl. Mater. Interfaces* **2021**, *13*, 47717–47727, doi:10.1021/acsami.1c15824.
43. Tang, F.; Guo, S.; Sun, Y.; Lin, X.; Qiu, J.; Cao, A. Facile Synthesis of Fe-Doped CoO Nanotubes as High-Efficient Electrocatalysts for Oxygen Evolution Reaction. *Small Struct.* **2022**, *3*, 2100211, doi:10.1002/sstr.202100211.
44. Deng, W.; Xie, W.; Li, D.; Gai, Y.; Chen, Z.; Yu, J.; Yang, R.; Bao, X.; Jiang, F. Controllable Tuning of Polymetallic Co-Ni-Ru-S-Se Ultrathin Nanosheets to Boost Electrocatalytic Oxygen Evolution. *NPG Asia Mater.* **2022**, *14*, 25, doi:10.1038/s41427-022-00373-9.
45. Cai, D.; Wang, D.; Wang, C.; Liu, B.; Wang, L.; Liu, Y.; Li, Q.; Wang, T. Construction of Desirable $NiCo_2S_4$ Nanotube Arrays on Nickel Foam Substrate for Pseudocapacitors with Enhanced Performance. *Electrochim. Acta* **2015**, *151*, 35–41, doi:10.1016/j.electacta.2014.11.040.
46. Song, Y.; Wang, Z.; Yan, Y.; Zhao, W.; Bakenov, Z. $NiCo_2S_4$ Nanoparticles Embedded in Nitrogen-Doped Carbon Nanotubes Networks as Effective Sulfur Carriers for Advanced Lithium–Sulfur Batteries. *Microporous Mesoporous Mater.* **2021**, *316*, 110924, doi:10.1016/j.micromeso.2021.110924.
47. Huang, Z.; He, W.; Shen, H.; Han, G.; Wang, H.; Su, P.; Song, J.; Yang, Y. $NiCo_2S_4$ Microflowers as Peroxidase Mimic: A Multi-Functional Platform for Colorimetric Detection of Glucose and Evaluation of Antioxidant Behavior. *Talanta* **2021**, *230*, 122337, doi:10.1016/j.talanta.2021.122337.
48. Tang, J.; Huang, W.; Lv, X.; Shi, Q. Improved Chemical Precipitation Prepared Rapidly $NiCo_2S_4$ with High Specific Capacitance for Supercapacitors. *Nanotechnology* **2021**, *32*, 085604, doi:10.1088/1361-6528/abc7d6.
49. Guo, Z.; Diao, Y.; Han, X.; Liu, Z.; Ni, Y.; Zhang, L. Mesoporous $NiCo_2Se_4$ Tube as an Efficient Electrode Material with Enhanced Performance for Asymmetric Supercapacitor Applications. *CrystEngComm* **2021**, *23*, 2099–2112, doi:10.1039/D0CE01778G.
50. Cai, P.; Huang, J.; Chen, J.; Wen, Z. Oxygen-Containing Amorphous Cobalt Sulfide Porous Nanocubes as High-Activity Electrocatalysts for the Oxygen Evolution Reaction in an Alkaline/Neutral Medium. *Angew. Chem.* **2017**, *129*, 4936–4939, doi:10.1002/ange.201701280.
51. Chen, N.; Du, Y.-X.; Zhang, G.; Lu, W.-T.; Cao, F.-F. Amorphous Nickel Sulfoselenide for Efficient Electrochemical Urea-Assisted Hydrogen Production in Alkaline Media. *Nano Energy* **2021**, *81*, 105605, doi:10.1016/j.nanoen.2020.105605.
52. Meng, A.; Yuan, X.; Shen, T.; Zhao, J.; Song, G.; Lin, Y.; Li, Z. Amorphous Nickel Sulfide Nanoparticles Anchored on N-Doped Graphene Nanotubes with Superior Properties for High-Performance Supercapacitors and Efficient Oxygen Evolution Reaction. *Nanoscale* **2020**, *12*, 4655–4666, doi:10.1039/C9NR09654J.
53. Wang, H.-Y.; Hsu, Y.-Y.; Chen, R.; Chan, T.-S.; Chen, H.M.; Liu, B. Ni^{3+} -Induced Formation of Active NiOOH on the Spinel Ni-Co Oxide Surface for Efficient Oxygen Evolution Reaction. *Adv. Energy Mater.* **2015**, *5*, 1500091, doi:10.1002/aenm.201500091.
54. Wang, Q.; Shang, L.; Shi, R.; Zhang, X.; Zhao, Y.; Waterhouse, G.I.N.; Wu, L.-Z.; Tung, C.-H.; Zhang, T. NiFe Layered Double Hydroxide Nanoparticles on Co,N-Codoped Carbon Nanoframes as Efficient Bifunctional Catalysts for Rechargeable Zinc-Air Batteries. *Adv. Energy Mater.* **2017**, *7*, 1700467, doi:10.1002/aenm.201700467.
55. Biesinger, M.C.; Payne, B.P.; Grosvenor, A.P.; Lau, L.W.M.; Gerson, A.R.; Smart, R.St.C. Resolving Surface Chemical States in XPS Analysis of First Row Transition Metals, Oxides and Hydroxides: Cr, Mn, Fe, Co and Ni. *Appl. Surf. Sci.* **2011**, *257*, 2717–2730, doi:10.1016/j.apsusc.2010.10.051.
56. Yamashita, T.; Hayes, P. Analysis of XPS Spectra of Fe^{2+} and Fe^{3+} Ions in Oxide Materials. *Appl. Surf. Sci.* **2008**, *254*, 2441–2449, doi:10.1016/j.apsusc.2007.09.063.
57. Yin, L.I.; Yellin, E.; Adler, I. X-Ray Excited *LMM* Auger Spectra of Copper, Nickel, and Iron. *J. Appl. Phys.* **1971**, *42*, 3595–3600, doi:10.1063/1.1660775.
58. He, Y.; Liu, X.; Chen, G.; Pan, J.; Yan, A.; Li, A.; Lu, X.; Tang, D.; Zhang, N.; Qiu, T.; et al. Synthesis of Co(II)-Fe(III) Hydroxide Nanocones with Mixed Octahedral/Tetrahedral Coordination toward Efficient Electrocatalysis. *Chem. Mater.* **2020**, *32*, 4232–4240, doi:10.1021/acs.chemmater.0c00512.
59. Li, J.; Cui, H.; Du, X.; Zhang, X. The Controlled Synthesis of Nitrogen and Iron Co-Doped Ni_3S_2@NiP_2 Heterostructures for the Oxygen Evolution Reaction and Urea Oxidation Reaction. *Dalton Trans.* **2022**, *51*, 2444–2451, doi:10.1039/D1DT03933D.
60. Huang, H.; Ning, S.; Xie, Y.; He, Z.; Teng, J.; Chen, Z.; Fan, Y.; Shi, J.; Barboiu, M.; Wang, D.; et al. Synergistic Modulation of Electronic Interaction to Enhance Intrinsic Activity and Conductivity of Fe–Co–Ni Hydroxide Nanotube for Highly Efficient Oxygen Evolution Electrocatalyst. *Small* **2023**, 2302272, doi:10.1002/smll.202302272.

61. Yang, L.; Qin, H.; Dong, Z.; Wang, T.; Wang, G.; Jiao, L. Metallic S-CoTe with Surface Reconstruction Activated by Electrochemical Oxidation for Oxygen Evolution Catalysis. *Small* **2021**, *17*, 2102027, doi:10.1002/smll.202102027.
62. Shinagawa, T.; Garcia-Esparza, A.T.; Takanabe, K. Insight on Tafel Slopes from a Microkinetic Analysis of Aqueous Electrocatalysis for Energy Conversion. *Sci Rep* **2015**, *5*, 13801, doi:10.1038/srep13801.
63. Li, G.; Anderson, L.; Chen, Y.; Pan, M.; Abel Chuang, P.-Y. New Insights into Evaluating Catalyst Activity and Stability for Oxygen Evolution Reactions in Alkaline Media. *Sustain. Energy Fuels.* **2018**, *2*, 237–251, doi:10.1039/C7SE00337D.
64. Anantharaj, S.; Sugime, H.; Noda, S. Why Shouldn't Double-Layer Capacitance (Cdl) Be Always Trusted to Justify Faradaic Electrocatalytic Activity Differences? *J. Electroanal. Chem.* **2021**, *903*, 115842, doi:10.1016/j.jelechem.2021.115842.
65. Shang, X.; Chen, W.; Jiang, Z.-J.; Song, C.; Jiang, Z. *In Situ* Growth of SeO_x Films on the Surface of Ni–Fe–Selenide Nanosheets as Highly Active and Stable Electrocatalysts for the Oxygen Evolution Reaction. *Mater. Adv.* **2022**, *3*, 2546–2557, doi:10.1039/D1MA01208H.
66. Anantharaj, S.; Kundu, S.; Noda, S. "The Fe Effect": A Review Unveiling the Critical Roles of Fe in Enhancing OER Activity of Ni and Co Based Catalysts. *Nano Energy* **2021**, *80*, 105514, doi:10.1016/j.nanoen.2020.105514
67. Kuai, C.; Xi, C.; Hu, A.; Zhang, Y.; Xu, Z.; Nordlund, D.; Sun, C.-J.; Cadigan, C.A.; Richards, R.M.; Li, L.; et al. Revealing the Dynamics and Roles of Iron Incorporation in Nickel Hydroxide Water Oxidation Catalysts. *J. Am. Chem. Soc.* **2021**, *143*, 18519–18526, doi:10.1021/jacs.1c07975.
68. Trotochaud, L.; Young, S.L.; Ranney, J.K.; Boettcher, S.W. Nickel–Iron Oxyhydroxide Oxygen-Evolution Electrocatalysts: The Role of Intentional and Incidental Iron Incorporation. *J. Am. Chem. Soc.* **2014**, *136*, 6744–6753, doi:10.1021/ja502379c.
69. Yang, M.; Lu, W.; Jin, R.; Liu, X.-C.; Song, S.; Xing, Y. Superior Oxygen Evolution Reaction Performance of Co_3O_4/$NiCo_2O4$ /Ni Foam Composite with Hierarchical Structure. *ACS Sustain. Chem. Eng.* **2019**, *14*, 12214–12221, acssuschemeng.9b01535, doi:10.1021/acssuschemeng.9b01535.
70. Chuah, X.-F.; Hsieh, C.-T.; Huang, C.-L.; Senthil Raja, D.; Lin, H.-W.; Lu, S.-Y. In-Situ Grown, Passivator-Modulated Anodization Derived Synergistically Well-Mixed Ni–Fe Oxides from Ni Foam as High-Performance Oxygen Evolution Reaction Electrocatalyst. *ACS Appl. Energy Mater.* **2019**, *2*, 743–753, doi:10.1021/acsaem.8b01794.
71. Duan, J.-J.; Zhang, R.-L.; Feng, J.-J.; Zhang, L.; Zhang, Q.-L.; Wang, A.-J. Facile Synthesis of Nanoflower-like Phosphorus-Doped Ni_3S_2/$CoFe_2O_4$ Arrays on Nickel Foam as a Superior Electrocatalyst for Efficient Oxygen Evolution Reaction. *J. Colloid Interface Sci.* **2021**, *581*, 774–782, doi:10.1016/j.jcis.2020.08.005.
72. Xue, Z.; Wang, Y.; Yang, M.; Wang, T.; Zhu, H.; Rui, Y.; Wu, S.; An, W. In-Situ Construction of Electrodeposited Polyaniline/Nickel-Iron Oxyhydroxide Stabilized on Nickel Foam for Efficient Oxygen Evolution Reaction at High Current Densities. International *Int. J. Hydrog.* **2022**, *47*, 34025–34035, doi:10.1016/j.ijhydene.2022.08.023
73. Zhao, T.; Wang, Y.; Chen, X.; Li, Y.; Su, Z.; Zhao, C. Vertical Growth of Porous Perovskite Nanoarrays on Nickel Foam for Efficient Oxygen Evolution Reaction. *ACS Sustain. Chem. Eng.* **2020**, *8*, 4863–4870, doi:10.1021/acssuschemeng.0c00060.
74. Gao, W.; Ma, F.; Wang, C.; Wen, D. Ce Dopant Significantly Promotes the Catalytic Activity of Ni Foam-Supported Ni_3S_2 Electrocatalyst for Alkaline Oxygen Evolution Reaction. *J. Power Sources* **2020**, *450*, 227654, doi:10.1016/j.jpowsour.2019.227654.
75. Kim, D.Y.; Lee, H.; Choi, S.R.; Choi, S.; An, W.Y.; Cho, H.-S.; Choi, M.; Park, J.-Y. Synthesis of Hierarchically Porous Ni Foam-Supported Heazlewoodite Ni_3S_2 Nanorod Electrocatalysts for Highly Efficient Oxygen Evolution Reaction. *J. Alloys Compd.* **2022**, *914*, 165305, doi:10.1016/j.jallcom.2022.165305.
76. Tao, K.; Gong, Y.; Zhou, Q.; Lin, J. Nickel Sulfide Wrapped by Porous Cobalt Molybdate Nanosheet Arrays Grown on Ni Foam for Oxygen Evolution Reaction and Supercapacitor. *Electrochim. Acta* **2018**, *286*, 65–76, doi:10.1016/j.electacta.2018.07.206.
77. Sun, Z.; Yuan, M.; Lin, L.; Yang, H.; Li, H.; Sun, G.; Yang, X.; Ma, S. Needle Grass-like Cobalt Hydrogen Phosphate on Ni Foam as an Effective and Stable Electrocatalyst for the Oxygen Evolution Reaction. *Chem. Commun.* **2019**, *55*, 9729–9732, doi:10.1039/C9CC03929E.
78. Li, X.; Han, G.-Q.; Liu, Y.-R.; Dong, B.; Hu, W.-H.; Shang, X.; Chai, Y.-M.; Liu, C.-G. NiSe@NiOOH Core–Shell Hyacinth-like Nanostructures on Nickel Foam Synthesized by in Situ Electrochemical Oxidation as an Efficient Electrocatalyst for the Oxygen Evolution Reaction. *ACS Appl. Mater. Interfaces* **2016**, *8*, 20057–20066, doi:10.1021/acsami.6b05597.
79. Zhang, Y.; Guo, P.; Niu, S.; Wu, J.; Wang, W.; Song, B.; Wang, X.; Jiang, Z.; Xu, P. Magnetic Field Enhanced Electrocatalytic Oxygen Evolution of NiFe-LDH/Co_3O_4 P-n Heterojunction Supported on Nickel Foam. *Small Methods* **2022**, *6*, 2200084, doi:10.1002/smtd.202200084.
80. Lv, Y.; Duan, S.; Zhu, Y.; Yin, P.; Wang, R. Enhanced OER Performances of Au@$NiCo_2S_4$ Core-Shell Heterostructure. *Nanomater.* **2020**, *10*, 611, doi:10.3390/nano10040611.
81. Feng, X.; Jiao, Q.; Chen, W.; Dang, Y.; Dai, Z.; Suib, S.L.; Zhang, J.; Zhao, Y.; Li, H.; Feng, C. Cactus-like $NiCo_2S_4$@NiFe LDH Hollow Spheres as an Effective Oxygen Bifunctional Electrocatalyst in Alkaline Solution. *Appl. Catal. B.* **2021**, *286*, 119869, doi:10.1016/j.apcatb.2020.119869.
82. He, B.; Song, J.-J.; Li, X.-Y.; Xu, C.-Y.; Li, Y.-B.; Tang, Y.-W.; Hao, Q.-L.; Liu, H.-K.; Su, Z. A Nitrogen-Doped $NiCo_2S_4$/CoO Hollow Multi-Layered Heterostructure Microsphere for Efficient Oxygen Evolution in Zn–Air Batteries. *Nanoscale* **2021**, *13*, 810–818, doi:10.1039/D0NR07120J.
83. Zheng, L.; Wang, S.; Wang, Y.; Zhao, Z.; Yang, P.; Song, J.; Shi, X.; Zheng, H. Cooperative Effect of Bimetallic MOF-Derived $CoNi(OH)_2$@$NiCo_2S_4$ Nanocomposite Electrocatalysts with Boosted Oxygen Evolution Activity. *Nanotechnology* **2022**, *33*, 265701, doi:10.1088/1361-6528/ac5f99.

84. Mohamed, S.G.; Hussain, I.; Shim, J.-J. One-Step Synthesis of Hollow C-$NiCo_2S_4$ Nanostructures for High-Performance Supercapacitor Electrodes. *Nanoscale* **2018**, *10*, 6620–6628, doi:10.1039/C7NR07338K.
85. Pu, J.; Cui, F.; Chu, S.; Wang, T.; Sheng, E.; Wang, Z. Preparation and Electrochemical Characterization of Hollow Hexagonal $NiCo_2S_4$ Nanoplates as Pseudocapacitor Materials. *ACS Sustain. Chem. Eng.* **2014**, *2*, 809–815, doi:10.1021/sc400472z.
86. Zou, J.; Xie, D.; Zhao, F.; Wu, H.; Niu, Y.; Li, Z.; Zou, Q.; Deng, F.; Zhang, Q.; Zeng, X. Microwave Rapid Synthesis of Nickel Cobalt Sulfides/CNTs Composites as Superior Cycling Ability Electrode Materials for Supercapacitors. *J. Mater. Sci.* **2021**, *56*, 1561–1576, doi:10.1007/s10853-020-05257-3.
87. Bao, Y.; Zhang, W.; Yun, T.; Dai, J.; Li, G.; Mao, W.; Guan, M.; Zhuang, Y. The Application of Transition Metal Sulfide Ni_3S_4/CNFs in Rechargeable Ni–Zn Batteries. *New J. Chem.* **2021**, *45*, 22491–22496, doi:10.1039/D1NJ03768D.
88. Kung, C.-W.; Chen, H.-W.; Lin, C.-Y.; Huang, K.-C.; Vittal, R.; Ho, K.-C. CoS Acicular Nanorod Arrays for the Counter Electrode of an Efficient Dye-Sensitized Solar Cell. *ACS Nano* **2012**, *6*, 7016–7025, doi:10.1021/nn302063s.
89. Khani, H.; Wipf, D.O. Iron Oxide Nanosheets and Pulse-Electrodeposited Ni–Co–S Nanoflake Arrays for High-Performance Charge Storage. *ACS Appl. Mater. Interfaces* **2017**, *9*, 6967–6978, doi:10.1021/acsami.6b11498.
90. Matoba, M.; Anzai, S.; Fujimori, A. Thermal Expansion, Thermoelectric Power, and XPS Studyof the Nonmetal-Metal Transition in $Ni_{1-x}S_{1-y}Se_y$. *J. Phys. Soc. Jpn.* **1991**, *60*, 4230–4244, doi:10.1143/JPSJ.60.4230.
91. Shi, Z.-T.; Kang, W.; Xu, J.; Sun, L.-L.; Wu, C.; Wang, L.; Yu, Y.-Q.; Yu, D.Y.W.; Zhang, W.; Lee, C.-S. In Situ Carbon-Doped $Mo(Se_{0.85}S_{0.15})_2$ Hierarchical Nanotubes as Stable Anodes for High-Performance Sodium-Ion Batteries. *Small* **2015**, *11*, 5667–5674, doi:10.1002/smll.201501360.
92. Danilson, M.; Altosaar, M.; Kauk, M.; Katerski, A.; Krustok, J.; Raudoja, J. XPS Study of CZTSSe Monograin Powders. *Thin Solid Films* **2011**, *519*, 7407–7411, doi:10.1016/j.tsf.2010.12.165.
93. Zou, X.; Wu, Y.; Liu, Y.; Liu, D.; Li, W.; Gu, L.; Liu, H.; Wang, P.; Sun, L.; Zhang, Y. In Situ Generation of Bifunctional, Efficient Fe-Based Catalysts from Mackinawite Iron Sulfide for Water Splitting. *Chem* **2018**, *4*, 1139–1152, doi:10.1016/j.chempr.2018.02.023.
94. Sahoo, M.K.; Samantara, A.K.; Behera, J.N. In Situ Transformed Cobalt Metal–Organic Framework Electrocatalysts for the Electrochemical Oxygen Evolution Reaction. *Inorg. Chem.* **2020**, *59*, 12252–12262, doi:10.1021/acs.inorgchem.0c01300.